

Approaching Lithium BEC with a Mini Trap

A Dissertation
Presented to the Faculty of the Graduate School
of
Yale University
in Candidacy for the Degree of
Doctor of Philosophy

by
Ruquan Wang

Dissertation Director: Prof. Mark Kasevich

May 2006

Copyright © 2007 by Ruquan Wang

All rights reserved.

Abstract

Approaching Lithium BEC with a Mini Trap

Ruquan Wang

2007

I will discuss the various experimental techniques to achieve BEC of bosonic ^7Li . The emphasis is on the Mini trap.

A Mini trap is a DC Ioffe-Pritchard type of magnetic trap of a few millimeters scale. With a size much smaller than the traditional magnetic trap, it has a comparable confinement, but dissipates 2-3 orders of magnitude less power. At 100A, it dissipates about 7W and has a trap depth of 70G. Because its trapping volume is comparable to the size of the MOT, an effective transfer from the MOT to the magnetic trap is easily achieved. We can easily transfer 2×10^8 atoms to the trap, which is 2 orders of magnitude more than a typical Micro trap. The Mini trap is immunized to the surface interaction problem of Micro trap. Its trap life-time is about 90 seconds at 78A while a typical Micro trap life-time is only 5 seconds.

Also mentioned is a proposed broadband optical slower. The unique advantage of the broadband optical slower is that we can achieve transverse cooling and longitudinal slowing at the same time, which can increase the cold atom beam flux by 2 orders of magnitude. Broadband optical slower does not need a strong magnetic field, unlike the Zeeman slower, which can be very important for precise measurement experiments.

Acknowledgements

I am grateful to my advisor, Professor Mark Kasevich, for his great insight and help over the past six years. It has been a privilege to work in his group.

I am also grateful to my Postdoc, Francesco Minardi, for the pleasant exchange of knowledge and ideas over the past 2 years as we worked together to design and build the experiment. I thank Mingchang Liu for the great job in keeping the experiment going while I was writing my thesis.

I would also like to thank my lab-mate Fabio Peixoto for his help over the few past years as we worked together on the experiment, my previous Postdoc, Gilles Nogues, for his work in setting up the transverse cooling, and my first Postdoc, Wayne Rowlands, for his help in the early days of my work in the lab.

I thank Kai Bongs, Jeff Fixler, Jeff McGuirk, Yvan Sortais, and Ari Tuchman for their helpful discussion.

I am grateful to my parents who gave me tremendous support, and to my sister who has always stood behind me when I needed her.

Contents

1	Introduction	1
1.1	Laser Cooling and BEC	1
1.2	Format of the Dissertation	3
2	Laser Cooling and Trapping of Neutral Atoms	5
2.1	Laser Cooling	5
2.1.1	Doppler Cooling	5
2.1.2	Sub-Doppler Cooling	8
2.1.3	Sub-Recoil Cooling	9
2.2	Magneto Optical Trap	9
2.2.1	Principle of Work	9
2.2.2	Trap Losses and the Number of Atoms in the MOT	12
2.2.3	Loading of the MOT, Loading Rate of the Zeeman Slower	14
2.2.4	Loading from a Vapor Cell	16
2.2.5	Transverse Cooling	17
2.2.6	A Novel Broad-Band Slower	17
3	Magnetic Trapping	20
3.1	Spherical Quadruple Trap	21
3.2	TOP Trap	22

3.3	Ioffe-Pritchard Trap	25
3.4	Scaling Law	27
3.5	Micro Traps	29
3.6	Lithium Elastic Collision Cross-Section	31
3.7	The Mini-Trap	33
3.8	Transferring Atoms to the Magnetic Trap	34
3.9	Semi-Adiabatic Transfer to the Mini-Trap	36
4	Evaporative Cooling	40
5	Experimental Setup	42
5.1	Overview	42
5.2	Lithium Energy Level Scheme and Laser Setup	42
5.3	Construction of an Extended Cavity Diode Laser	45
5.4	Vacuum Design	48
5.5	Mini-Trap Construction	50
5.6	MOT Coils and Transfer Coils Assembly	52
5.7	Power Supply and Current Switches	54
5.8	Timing and Control System	59
5.9	Imaging System	61
5.9.1	Fluorescent Imaging	62
5.9.2	Absorption imaging	64
5.9.3	Temperature Measurement from Free Expansion	67
5.10	RF Evaporative Cooling Set-up	68
5.10.1	Temperature Measurement with RF Cut	70
6	Experimental Results	73
6.1	Computer Simulation of the Mini-Trap	73

6.2	Vacuum Baking	76
6.3	MOT Loading	77
6.4	Doppler Cooling	80
6.5	Optical Pumping	81
6.6	Transfer to the Mini-Trap	82
6.7	Trap Life Time in the Mini-Trap	85
6.8	RF Cut and Trap Parameters	87
6.9	Absorption Imaging	90
6.10	Evaporative Cooling	92
6.11	Trap Oscillation Frequency Measurement With Parametric Heating	94
6.12	Phase Space Density Towards BEC	97
7	Conclusion and Outlook	100

List of Figures

2.1	A typical MOT configuration	10
2.2	1D-MOT configuration	11
2.3	A Typical Zeeman Slower Configuration	15
2.4	A Transverse Cooling Stage in Front of a Zeeman Slower	17
2.5	A broad band slower	18
3.1	Spherical Quadruple Trap	21
3.2	Spherical Quadruple Trap Field and Potential	22
3.3	TOP	23
3.4	A Typical Ioffe-Pritchard Trap	26
3.5	2-D Micro-Trap	29
3.6	2-D Micro-Trap Field in the Radial Direction	30
3.7	3-D Micro-Trap	31
3.8	3-D Micro-Trap Axial Field	32
3.9	minitrp	34
3.10	The QUIC Trap Geometry	36
3.11	The QUIC Trap Field Plot	37
3.12	The trap setup. 1.MOT coils 2.Lower rectangular coils 3.Upper rectangular coils 4.The negative lead of the Mini-Trap 5.The positive lead of the Mini-Trap 6.Mini-Trap 7.Vacuum chamber	39

5.1	Lithium Energy Level Scheme	44
5.2	Laser Setup	45
5.3	A Home-made Piezo Stack	47
5.4	Vacuum Setup	49
5.5	The Copper Piece	50
5.6	The DBC Chip	51
5.7	The - Current Lead and The Heat Sink	53
5.8	the + current lead	54
5.9	The Assembly Diagram	55
5.10	Schematics for the MOT Coils	56
5.11	Schematics for the Mini-Trap	57
5.12	Schematics for the Pumping Bias Coil and the Rectangular Coils	58
5.13	The Timing System	59
5.14	The camera diagram	61
5.15	Fluorescent Imaging	62
5.16	Fluorescent Imaging in the Mini-Trap	64
5.17	Absorption Imaging in the Mini-Trap	65
5.18	the RF Frequency Synthesizer	69
5.19	Antenna	70
5.20	Energy Diagram	71
5.21	RF Cut Plot	72
6.1	The Field of the Mini-Trap in the x Direction	74
6.2	The Field of the Mini-Trap in the y Direction	74
6.3	The Field of the Mini-Trap in the Axial Direction	75
6.4	Loading Rate Measurement	78
6.5	The Power Split and Combination of the Comb and Molasses Beam	80

6.6	Optical Pumping Setup	83
6.7	Timing Sequence of the Current Ramps	83
6.8	The Oscillation of Atom Cloud in the Mini-Trap	84
6.9	the decay of atoms in the Mini-Trap	85
6.10	Comparison of Trap Life Time at Different Current	86
6.11	The Sudden Jump of Atom Numbers After the Cut	88
6.12	Mini-Trap Current vs. the Bottom Frequency	89
6.13	RF Cut and Temperature Measurement	89
6.14	False Color Image of Absorption Image	91
6.15	Gaussian Fit of the Cloud Optical Density. Note the horizontal fit only have half of the cloud because the other half of the trap is blocked by the vacuum chamber.	91
6.16	Absorption vs. Detuning	92
6.17	RF Cooling Ramp	93
6.18	In the Axial Direction, $\omega = \omega_0$	95
6.19	In the Radial Direction, $\omega = \omega_0$	95
6.20	In the Axial Direction, $\omega = 2\omega_0$	96
6.21	In the Radial Direction, $\omega = 2\omega_0$	96
6.22	The absorption images at the final stage of the evaporative cooling. Because almost all of the upper half of the Mini-Trap is blocked by the chamber, we can only see half of the atom cloud. The absorption images is cut at the center. When the cloud is sufficiently small, we can see the whole atom cloud, as shown in the bottom picture. The center of the trap is decided at this stage.	98
6.23	Phase space density vs number of atoms	99

Chapter 1

Introduction

1.1 Laser Cooling and BEC

In the past two decades, our ability to cool and trap atoms with laser light and magnetic fields has advanced considerably. In 1985, S. Chu et al. [1] demonstrated the first laser cooling experiment which cooled sodium atoms down to the Doppler temperature of $240\mu K$; this is a significant improvement compared to previous cryogenic cooling techniques. Subsequent experiments by W. Phillips et al. [2] demonstrated temperatures much lower than the Doppler temperature and stimulated both the experimental and theoretical exploration [3] of sub-Doppler cooling. This new cooling mechanism produced temperatures of the order of $10^{-5}K$. In 1987, S. Chu demonstrated the world's first magneto-optical trap (MOT) [4], which not only cooled, but also trapped atoms. A typical MOT traps 10^9 atoms, with a temperature of order $100\mu K$ and a density of $10^{11}cm^{-3}$, limited by the existence of near resonant light. What distinguishes laser cooling from velocity selection is the increase in phase space density $n\lambda_{dB}^3$, where n is the density and λ_{dB} is the thermal de Broglie wavelength of the atoms. The phase space density of the MOT is 10^{12} higher than that of a typical thermal atomic beam. The MOT is very easy to set up and becomes the basic building block for many precision measurement experiments. One of the most

important experiment is the fountain clock [5], which has become the standard for the next generation atomic clocks.

When the phase space density of a cloud of free Boson gas reaches 2.62, the gas will go through a phase transition, and a macroscopic portion of the atoms will stay in the ground state and form a coherent macroscopic matter wave function, similar to a laser, which is a coherent electromagnetic wave function. In 1986, Harald Hess [51] suggested that evaporative cooling can be used to cool Hydrogen and achieve BEC. The idea is to trap the atoms in a magnetic trap and use forced evaporative cooling to increase the phase space density. The phase space density of the MOT is about 10^{-6} , still 6 orders of magnitude lower than that is needed to reach BEC, but it is a good starting point for forced evaporative cooling, and the apparatus is much easier to set up than the cryogenic system for the Hydrogen BEC experiment. Combining the laser cooling and trapping technique, and the magnetic trapping [19] and forced evaporative cooling technique, BEC in Rubidium, Lithium, and Sodium were simultaneously achieved in 1995 [6, 7, 8].

Since evaporative cooling uses elastic collision to generate cold atoms, the most important parameter for evaporative cooling is the elastic collision cross-section. Among all the alkaline elements, ^{87}Rb and ^{23}Na have an order of magnitude bigger elastic collision cross-sections than ^7Li , so the majority of BEC experiments in the world work with ^{87}Rb or ^{23}Na ; only 2 groups have achieved BEC in ^7Li so far with evaporative cooling in magnetic traps. Tight confinement of the magnetic trap, a large number of atoms to start evaporative cooling, and long trap lifetime are very important in achieving Lithium BEC.

We designed a magnetic trap that gives us a very tight confinement, a large trapping volume, and long trap lifetime. Compared with large, traditional TOP and Ioffe-Pritchard traps, it has better trap confinement at 2 orders of magnitude lower power dissipation. Compared with the Microtrap, it has a much larger trapping volume and can trap 2 orders of magnitude more atoms. Also it has a very long life time about 90 seconds, much longer than the 5 second lifetime of typical Micro traps.

^7Li is interesting because unlike most of the other alkalies, it has a negative scattering length, the atoms are attracted to each other, and when Lithium BEC is loaded in an optical lattice, the ground states will be that all the atoms stay in one potential well. Since the energy of atoms stay in different wells are degenerate, the ground state of this system is a superposition of these ground states, which is a Schrödinger cat [9]. Our short-term goal is to get Li BEC and load it into the optical lattice and study the properties of this Schrödinger cat.

Another interesting subject is the fermionic ^6Li . Recently, there has been a breakthrough in using Feshbach resonance [10, 11, 12, 13] to form fermion pairs and reach the condensation of fermion pairs. [14, 15, 16, 17] Our long-term goal is to use the sympathetic cooling of ^6Li and ^7Li to get quantum degenerate ^6Li and get the condensate of the ^6Li pairs with Feshbach resonance and evaporative cooling.

1.2 Format of the Dissertation

In Chapters 2, 3, and 4, I provide a simple but adequate introduction of the most important techniques of getting BEC. The introduction focuses on important considerations when designing a BEC apparatus, and important formulae are quoted from books or papers listed in the citation. Chapter 2 will discuss laser cooling and trapping, and focus of the chapter is on how to improve the loading rate of the MOT and capture the maximum number of atoms in the MOT. Chapter 3 discuss magnetic trapping, and its focus is on the relative advantages and disadvantages of various kinds of magnetic traps. Chapter 3 gives a simple discussion on the theory of evaporative cooling. One of the most important threshold conditions of sustainable evaporative cooling is quoted in this chapter. This condition must be satisfied by a BEC apparatus.

In Chapter 5, there is a detailed description of our experiment setup. They include the optics setup, vacuum chamber design, and Mini Trap design. Also mentioned is a home-

made extended cavity diode laser. We use a two-Piezo system to reduce the noise of the laser, and we designed an automatic lock circuit to lock the laser more easily. In Chapter 6, the results of our experiment are presented. Using our Mini Trap, we successfully reached the phase space density of a BEC.

Chapter 2

Laser Cooling and Trapping of Neutral Atoms

2.1 Laser Cooling

2.1.1 Doppler Cooling

The possibility of using laser radiation to cool atoms was first proposed by Hansch and Schawlow in 1975 [18]. The principle of Doppler cooling is very easy to understand. In the 1-D case, atoms are cooled by two counter propagating laser beams which are a little red detuned from the atomic transition. When an atom is running towards one beam, due to the Doppler effect, it sees a higher frequency from the beam and the beam becomes closer to resonance of the atomic transition, whereas the beam the atom is running away from will be further away detuned from the resonance. The atom predominantly absorbs a photon from the beam it runs against and is slowed down by the photon momentum kicking against its speed. Now the atom will stay in the excited state. When the atom relaxes from the excited state with spontaneous emission, it emits a photon in a random direction, so that the average effect is that there is no momentum change for the atom.

Finally in the whole cycle, the atom is slowed down by one photon recoil $\hbar k$. As the cycle continues to go on and on, the atom is slowed down.

A quantitative treatment of this problem considers a 2-level atom interacting with a traveling beam of intensity I , and the scattering force is [20]:

$$F_{scat} = \frac{\hbar k \Gamma}{2} \left[\frac{I/I_{sat}}{1 + I/I_{sat} + 4(\Delta/\Gamma)^2} \right] \quad (2.1)$$

Where $k = 2\pi/\lambda$ is the wave vector of the light, $\Gamma = 1/\tau_e$ is the excited state line width, I is the laser intensity, $\Delta = \omega - \omega_0$ is laser detuning, and

$$I_{sat} = \frac{\hbar \omega \Gamma k^2}{12\pi} \quad (2.2)$$

is the saturation intensity.

For two counter propagating beams in the low intensity limit, considering the Doppler effect,

$$\Delta(v) = \Delta \pm kv. \quad (2.3)$$

where δ is the detuning of the laser. So the total force becomes

$$F_{total} = \frac{\hbar k \Gamma}{2} \left[\frac{I/I_{sat}}{1 + I/I_{sat} + \frac{4}{\Gamma^2}(\Delta + kv)^2} \right] - \frac{\hbar k \Gamma}{2} \left[\frac{I/I_{sat}}{1 + I/I_{sat} + \frac{4}{\Gamma^2}(\Delta - kv)^2} \right] \quad (2.4)$$

In the low velocity limit, the leading term of the Taylor expansion with respect to v gives the Doppler cooling force.

$$F_{total} = -\beta v \quad (2.5)$$

where

$$\beta = -4\hbar k^2 \frac{2I}{I_{sat}} \frac{2\Delta/\Gamma}{(1 + (2\Delta/\Gamma)^2)^2} \quad (2.6)$$

When the laser is red detuned, detuning Δ is negative, the force is a damping force, which gives the cooling effect.

The speed of the atom will not decelerate to $v = 0$ because of the quantum fluctuation of the cooling force. A simple argument can be used to find the low temperature limit of the Doppler cooling, as in [52].

First, from the conservation of energy and momentum, in the reference frame where the atom speed $v = 0$, we have for each absorption and spontaneous cycle,

$$\begin{aligned} \omega_{abs} &= \omega_0 + \vec{k}_{abs} \cdot \vec{v} + R/\hbar \\ \omega_{em} &= \omega_0 + \vec{k}_{em} \cdot \vec{v}' - R/\hbar \end{aligned} \quad (2.7)$$

where $|\vec{k}_{abs}| = \omega_{abs}/c$ is the wave vector of the absorbed photon, $|\vec{k}_{em}| = \omega_{em}/c$ is the wave vector of the emitted photon, $\omega = 2\pi\nu_0$ is the atomic resonant angular frequency, \vec{v} is the atom velocity in the ground state, \vec{v}' is the atom velocity in excited state, and $R = (\hbar k)^2/2M$ is the recoil energy.

Considering the average of $\vec{k}_{em} \cdot \vec{v}' = 0$ because of the random direction of the spontaneous emission, for each absorption and spontaneous emission cycle, the atomic kinetic energy change is

$$\Delta E_K(atom) = -\Delta E(photon) = -\hbar(\omega_{abs} - \omega_{em}) = \hbar\vec{k}_{abs} \cdot \vec{v} + 2R \quad (2.8)$$

Now, the first term is the same Doppler cooling force we discussed in the beginning of this section, and the second term is a heating term which describes the heating of the atom due to the photon scattering.

The energy change of the atom is

$$\frac{dE_x}{dt} = \frac{\Gamma}{2} \left[\frac{I/I_s}{1 + I/I_s + 4(\Delta_+/\Gamma)^2} (\hbar k v_x + 2R) + \frac{I/I_s}{1 + I/I_s + 4(\Delta_-/\Gamma)^2} (-\hbar k v_x + 2R) \right] \quad (2.9)$$

in which

$$\Delta_{\pm} = \Delta \pm k v. \quad (2.10)$$

Let $\frac{dE_x}{dt} = 0$ and assume laser intensity is much smaller than the saturate intensity, we can find the low speed limit of v and the corresponding low temperature limit of Doppler cooling

$$\frac{\hbar\Gamma}{8} \left(\frac{2|\Delta|}{\Gamma} + \frac{\Gamma}{2|\Delta|} \right) \quad (2.11)$$

when $\Delta = \Gamma/2$, Doppler cooling reaches the minimum temperature of $\frac{\hbar\Gamma}{4}$, typically about $100\mu K$.

Doppler cooling can effectively cool the atoms from room temperature down to about $100\mu K$ and reach a typical density limit of $10^{11} cm^{-3}$, which is about 6 orders of magnitude smaller in phase space density that is needed to reach BEC.

2.1.2 Sub-Doppler Cooling

Sub-Doppler cooling, also known as sisyphus cooling, are cooling mechanisms using the polarization gradient of the cooling light. They can cool atoms down to about $10\mu K$ and they can easily be set up with the molasses configuration, so they become a standard in getting Rubidium and Sodium BEC. However, Sub-Doppler cooling does not work well with Lithium because the excited states energy level split is comparable to the line width, and the optical pumping which the Sub-Doppler cooling requires does not work very well.

2.1.3 Sub-Recoil Cooling

Usually referred to as Raman cooling [21] and VSCPT [22], these cooling methods can cool atoms below the recoil limit. However, because these cooling mechanisms do not work very well in high density atomic samples, they never became a popular pre-cooling approach. A new cooling approach called degenerate Raman sideband cooling [53] is very interesting because it can cool 10^7 atoms to $2.8\mu K$ at a density of $1.4 * 10^{13} cm^{-3}$, corresponding to a phase density of 1/180.

2.2 Magneto Optical Trap

MOT (Magneto Optical Trap) is one of the key technologies in getting BEC. It is very similar to the Optical Molasses with an additional pair of anti-Helmholtz coils to make the scattering force from the laser cooling beams dependent on the position of the atoms.

A typical MOT set-up is shown in Fig. 2.1. A pair of anti-Helmholtz coils apply a low B-field gradient, typically about 10G/cm. 3 pairs of red detuned counter propagating σ^+ and σ^- beams give the atoms both cooling and spatial confinement forces. Because it can collect atoms continually from background vapor or from an incoming slowed atom beam, and cool them to the Doppler or Sub-Doppler temperature, it has become the standard in most BEC experiments as the initial loading stage. MOT is pretty robust against trapping beam misalignment, intensity imbalance, and frequency detuning, and has a capture speed of about 10m/s, or 10mK trap depth.

2.2.1 Principle of Work

In order to understand how MOT works, we resort to the simplest case, that is, a 1-D MOT with a 2-level atom. The atom has a ground state of $F=0$ and an excited state of $F=1$, as shown in Fig. 2.2. Note that the σ^+ , σ^- light polarization and the magnetic quantum number m_F are all defined according to the z direction. The magnetic field

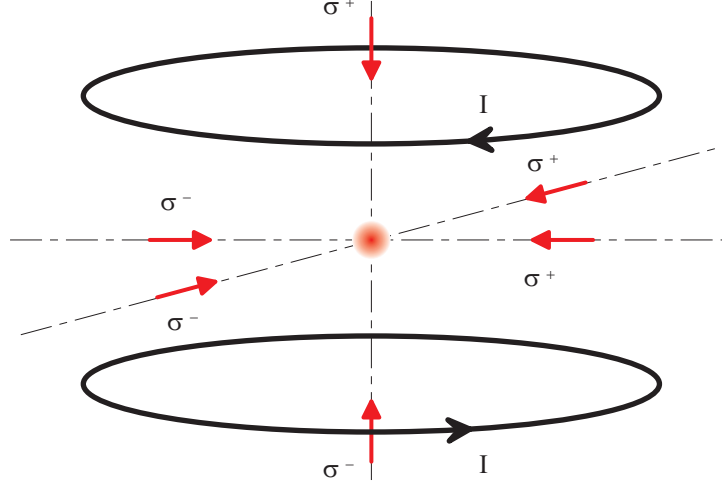


Figure 2.1: A typical MOT configuration

direction reverses when crossing the $z=0$ point, so the the magnetic quantum number does not refer to the local magnetic field. The excited states energy levels split because of the Zeeman effect. ω_0 is the free field atomic resonance frequency and ω is the trapping laser frequency, red detuned of $\delta = \omega_0 - \omega$ from the atomic frequency.

Now, a ground state atom interacts with both of the 2 beams. The blue or σ^+ beam will excite the atom to the $F = 1, m_F = 1$ state and the red or σ^- beam will excite the atom to the $F = 1, m_F = -1$ state. When the atom sits at $z < 0$, the blue or σ^+ beam, which excited the atoms to the $F = 1, m_F = 1$ states, is detuned closer to the resonant frequency, thus the atoms will more likely absorb a photon from it and get a kick in the z direction, and this will push the atom to the center. When the atom sits at $z > 0$, the red or σ^- beam, which excited the atoms to the $F = 1, m_F = -1$ states, is detuned closer to the resonant frequency, thus the atoms will more likely absorb a photon from it and get a kick in the negative z direction, and this will also push the atom to the center.

The simple theory can easily be extended to the MOT and gives the trapping and damping properties of the trap. The detuning now depends on not only the speed of atoms but also the position of the atoms due to the Zeeman shift.

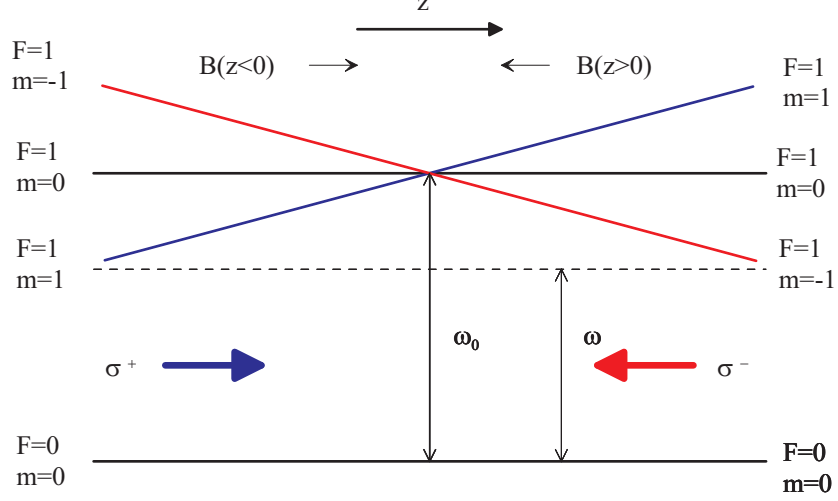


Figure 2.2: 1D-MOT configuration

$$\delta_{\pm} = \delta \mp kv \pm \mu B/\hbar \quad (2.12)$$

so

$$f_{total} = \frac{\hbar k \Gamma}{2} \left[\frac{I/I_{sat}}{1 + I/I_{sat} + \frac{4}{\Gamma^2}(\delta_+)^2} \right] - \frac{\hbar k \Gamma}{2} \left[\frac{I/I_{sat}}{1 + I/I_{sat} + \frac{4}{\Gamma^2}(\delta_-)^2} \right] \quad (2.13)$$

In the low velocity and weak field limit, the leading term of the Taylor expansion gives the Doppler cooling force.

$$f_{total} = -\beta v - \kappa r \quad (2.14)$$

where

$$\beta = -\hbar k^2 \frac{8(I/I_{sat})(\delta/\Gamma)}{(1 + (2\delta/\Gamma)^2)^2} \quad (2.15)$$

and

$$\kappa = \frac{\mu A}{\hbar k} \beta \quad (2.16)$$

Notice that including the Doppler cooling term, there is an additional spatial restoring force term. Under typical experimental conditions, the atomic motion under this force is heavily over damped.

For the 3-D case, we simply add the force in a different direction when the intensity of the laser beams are low. An important note is that if the magnetic field direction is not aligned with the laser beams, the polarization will be destroyed and the MOT performance will degrade or may not even work at all. Take a look at the 3-D MOT shown in Fig. 2.1. In the radial direction, the magnetic field is azimuthal symmetric and perpendicular to the symmetry axis, and this agrees with the direction of the laser beams. In the axial, the magnetic field is in the direction of the symmetry axis and again agrees with the laser beams. If the round coils are replaced by a pair of elliptical coils, the radial magnetic field is no longer azimuthal symmetric, and if the radial beams are aligned as is, the MOT will not work. In order for the MOT to work, the beams have to be aligned with the symmetry axis of the coil.

2.2.2 Trap Losses and the Number of Atoms in the MOT

The maximum number of atoms that can be loaded into the MOT is decided by the balance between the capturing rate and the loss rate. There are 2 major loss rates that are important.

The first one is the collision with the background gas. This is usually the biggest loss in a small MOT. In the case of loading directly from the vapor cell, the background gas is the same as the trapping atoms. In the case of the Zeeman slower loaded case, the background gas is the residue gas in the ultra high vacuum(UHV) chamber and mostly comprised of H_2 .

Loss from the background collision is proportional to the number of atoms in the trap.

$$\frac{dN(t)}{dt} = R_f - \gamma N(t) \quad (2.17)$$

where R_f is the loading rate, and γ is the background loss rate.

When loading from a vapor cell, MOT can capture all the 4π solid angle of the incoming atoms, and the loading rate is

$$R_f = \frac{nV^{2/3}v_c^4}{2u^3} \quad (2.18)$$

where n is the density of the atoms, $u = \sqrt{2K_b T/m}$, is the most probable velocity of the atoms with temperature T and v_c is the capture speed. When the MOT only captures part of the 4π solid angle, the loading rate has to take into account of the solid angle Ω

$$R_f = \frac{\Omega}{4\pi} \frac{nV^{2/3}v_c^4}{2u^3} \quad (2.19)$$

Eq. 2.17 has the solution

$$N(t) = \frac{R_f}{\gamma} (1 - e^{-\gamma t}) \quad (2.20)$$

It is easy to see that the final number in the trap is

$$N(t) = \frac{R_f}{\gamma} \quad (2.21)$$

The other important loss is the light-induced loss [23, 24]. A 2-atom collision assisted with light can release a very big kinetic energy to the atoms and eject them from the MOT. The losses depend on the density of atom square and limit the maximum density and number of trapped atoms.

$$\frac{dn}{dt} = -\gamma n - \beta n^2 \quad (2.22)$$

Theoretical work and a careful experimental study of the trap lifetime provide 2 dominant loss mechanisms, the fine structure changing collisions and radiative redistribution.

The fine structure changing collision happens when a ground state and a excited state

collide and are transferred into a ground state and the other fine structure of the excited state and release the fine structure split energy. This energy is usually large enough to eject both atoms from the trap. However, the fine structure split energy of Lithium is small enough so that a relatively strong MOT can suppress this loss channel.

The radiative redistribution happens when one ground state atom and an excited state atom attract or repel each other under a much stronger dipole interaction. This process accelerates the atoms and releases energy that is equal to the difference of the absorbed and emitted photon.

2.2.3 Loading of the MOT, Loading Rate of the Zeeman Slower

From Eq. 2.18 we can see that in order to get the maximum number of atoms loaded into the MOT, we have to maximize the density of the incoming atomic flux and minimize the trap loss.

Usually, the MOT is loaded from an atomic beam. However, the capture speed of a typical MOT is less than 50m/s, significantly below the average speed of atoms at 300K or higher. The low capture speed of the MOT is due to two reasons. Firstly, the line width of the laser is usually smaller than the line width of the atomic transition, and the line width of the atomic transition is about 10Mhz, much smaller than the Doppler shift of 300K atoms; the atoms will see a far detuned laser frequency due to the Doppler shift and as we can see from Eq. 2.1, the scattering force is very small. Secondly, the scattering force is saturated at $\frac{\Gamma}{2}\hbar k$. That means the deceleration rate is bounded. In order to stop an atom, a big laser beam is required. The typical size of the MOT beams is usually around one inch, not big enough to stop a 300K atom.

In order to solve this problem, many different loading schemes were invented, and one of the most successful schemes is the Zeeman slower [25] as shown in Fig. 2.3. A tapped magnet generates the slope of a magnetic field which compensates for the Doppler shift by the Zeeman shift. A slower beam shoot counter propagates to the incoming atomic beam

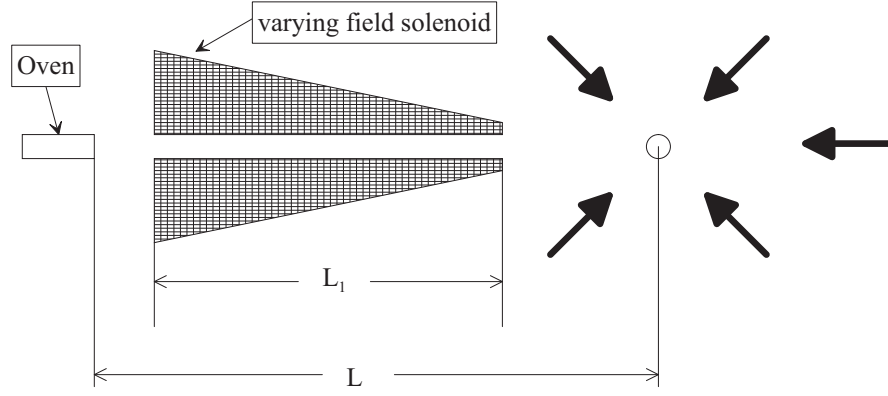


Figure 2.3: A Typical Zeeman Slower Configuration

before they reach the MOT capture area. The Zeeman slower works effectively to slow atoms with speed up to 500m/s or more.

From Eq. 2.19, it is easy to find

$$R_f \propto \Omega v^4 = \frac{Sv^4}{L^2} \quad (2.23)$$

where Ω is the solid angle of the capture area with respect to the oven and S is the capture area. The light slowing acceleration saturates at

$$a_{max} = \hbar k \Gamma / 2 \quad (2.24)$$

so that the capture speed is related to the length by

$$v^2 = 2a_{max}L_1 \quad (2.25)$$

and plugging into Eq. 2.23, we get

$$R_f \propto 2a_{max}S \frac{L_1^2}{L^2} \quad (2.26)$$

Surprisingly, when $L_1 \simeq L$ the fill rate is not related to the length of the Zeeman slower.

This goes strongly against the intuition that a longer Zeeman slower can stop faster atoms, so the fill rate of the MOT will be bigger. The scaling is even worse when the Zeeman slower is too long; the filling rate is no longer proportional to v_c^4 , and instead it drops sharply when v_c is close to the most probable speed.

However, in a typical experimental setup, $L \simeq L_1 + 20\text{cm}$ due to the vacuum setup and geometry limit. If there is no Zeeman slower, the equivalent L_1 will be the size of the MOT beam, which is roughly 2cm, from Eq. 2.26, the loading rate is 2 orders of magnitude smaller.

Another problem of the Zeeman slower is that the slowing is only in the longitudinal direction. As the longitudinal speed is slowed down, the transverse speed is heated up from the spontaneous emission of photons from the excited states. The transverse heating makes the capture solid angle even smaller.

2.2.4 Loading from a Vapor Cell

Another extreme design the MOT loading is to emphasize the capture solid angle and not to care too much about the capture speed. This is shown in the vapor cell MOT [26] set-up. The MOT is loaded directly from the background vapor, and the capture solid angle is 4π , about 3 orders of magnitude larger than a Zeeman slower design. A well-optimized MOT with far detuned light and big MOT beams can capture up to 50m/s atoms. The disadvantage of using the vapor cell MOT is that when the vapor pressure is higher, the filling rate is bigger, but the loss rate due to the background collision is also higher. According to Eq. 2.21, the final number of atoms depend both on the filling rate and the loss rate, and the effect of raised vapor pressure is canceled here. Also, the atoms will be transferred to the magnetic trap where they are stored and evaporative cooled. The vapor pressure is bad for the lifetime of the magnetic trap. The vapor cell MOT works effectively for atoms with a high vapor pressure under room temperature and heavy mass (so it has slower speed and less Doppler shift), such as in the case of Cesium and Rubidium.

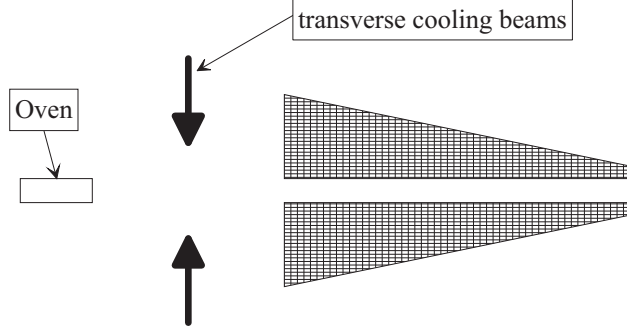


Figure 2.4: A Transverse Cooling Stage in Front of a Zeeman Slower

For Lithium, the temperature has to be raised to 600K to get a reasonable vapor pressure. It is hard to heat up the whole vapor cell to this high temperature.

2.2.5 Transverse Cooling

In the previous section, we saw that the capture solid angle of a Zeeman slower is smaller with a longer shower length and it scales so badly that it cancels the benefit gained from a higher capturing speed. We can fix this problem by adding a transverse cooling stage in front of the Zeeman slower as in [27, 28], shown in Fig. 2.4. This stage will collimate the incoming atomic beams and significantly increase the capture solid angle of the Zeeman slower. The result usually has a filling rate that is higher by 1 or 2 orders of magnitude.

2.2.6 A Novel Broad-Band Slower

The above-mentioned slower still has several disadvantages. First, the transverse cooling cannot stay inside a Zeeman slower, and there is still the transverse heating problem which limits the effective working length of the Zeeman slower. Second, the Zeeman slower generates a stray field which is hard to shield and bad for many precision measurement experiments.

The proposed broad-band slower is shown in Fig. 2.5.

Broad-band light was used to slow atoms before [54], but the major problem facing

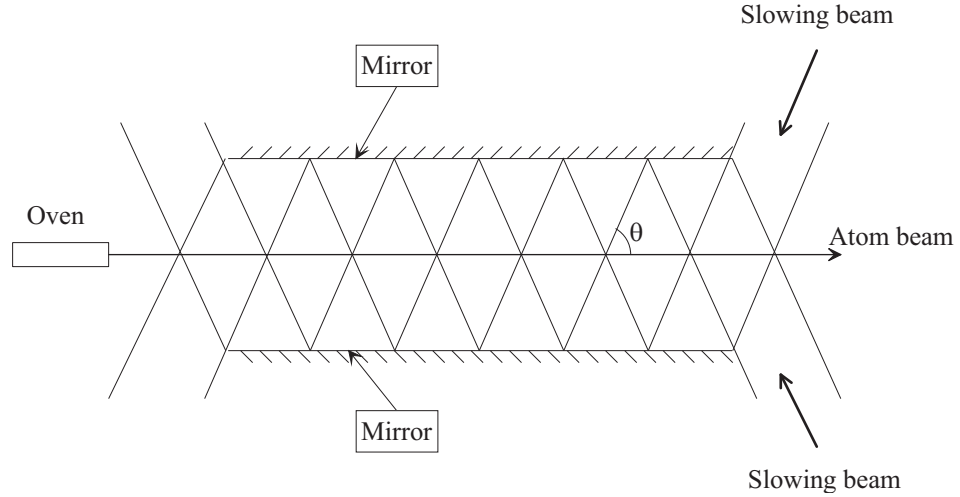


Figure 2.5: A broad band slower

this approach is that in order to saturate the transition for all the different frequencies, the slowing light power has to be very high. A band-width of 150Mhz is relatively easy to achieve, but in order to achieve a 500Mhz bandwidth to slow down atom speed so that is comparable to a typical Zeeman slower, the power is not easy to achieve. In the broadband slower shown above, the slowing light does not run counter propagating to the incoming atomic beam, instead the slowing light intersect with the atomic beam at an angle θ . For a given band-width of the slowing light Δ , this arrangement can slow atoms with speed up to

$$v = \frac{2\pi\Delta}{k\cos\theta} \quad (2.27)$$

effectively broaden the bandwidth by a factor of $1/\cos\theta$. If we choose $1/\cos\theta = 4$, we can use a 150Mhz band width light to slow Lithium atoms with speed of 400m/s, roughly comparable to the Zeeman slower capture range.

The most interesting thing is that this slower also do transverse cooling; in the beginning, this seems obvious, however, after a careful thought, we found that with an arbitrary broadband spectrum, it does not transversely cool atoms with a incoming angle that is smaller than $\pi/2 - \theta$. We have to shape the spectrum of the broad band light so that the

further detuning light has a greater intensity, and under this light, the transverse cooling works with any incoming atoms.

The biggest advantage of this slower is that it slows and transversely cools atoms simultaneously. This makes it possible to build a slower to slow all the atoms from the oven. Also, there is no magnet in this slower, so no stray fields are generated, which is very important for some precision measurement experiments.

The disadvantage of this slower is that the longitudinal cooling force is a factor of $1/\cos\theta$ smaller, so the length of the slower is a factor of $1/\cos\theta$ longer than the Zeeman slower.

Chapter 3

Magnetic Trapping

MOT has many limits, and the biggest one is the density and temperature limit. This makes the MOT cloud at a phase space density at about 10^{-6} , 6 orders of magnitude smaller than what is needed to reach the BEC.

In order to reach the BEC, a conservative trap is needed. Two major conservative traps are the magnetic trap and the far detuned dipole trap.

The magnetic trap uses a field minimum to trap low field seeking atoms. The advantages of the magnetic trap are its big trapping volume, deep trap depth, and long trap lifetime.

The far detuned optical dipole trap [29] uses a single or a cross pair of tightly focused laser beams to trap atoms. The trap potential is due to the spatial distribution of the intensity of the laser beams, which generate different AC stark shifts. The dipole trap has the advantage of tight confinement and has the ability to trap any atomic species. However, the dipole trap has a shallow trap depth and shorter trap lifetime due to photon scattering. It is also harder to align the optics.

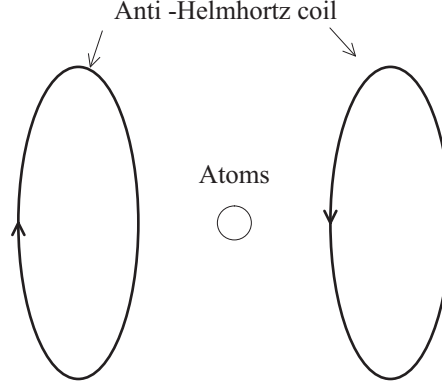


Figure 3.1: Spherical Quadruple Trap

3.1 Spherical Quadruple Trap

The simplest magnetic trap is the spherical Quadruple trap [30], as shown in Fig. 3.1. A pair of anti-Helmholtz coils generate a linear magnetic field.

The magnetic field crosses zero at the center. In the magnetic trap, the spin of an atom is aligned with the magnetic field, and the potential of the atoms is proportional to the magnitude of the magnetic field. Fig. 3.2 shows the magnetic field and the potential of the Quadruple trap.

For a Quadruple trap, the field gradient in the axial and radial direction are related by

$$B'_z = \frac{\partial B}{\partial z} = 2 \frac{\partial B}{\partial r} = B'_r \quad (3.1)$$

and the B field around the center of the trap is described as

$$\vec{B} = B'_z z \vec{e}_z + \frac{1}{2} B'_z x \vec{e}_x + \frac{1}{2} B'_z y \vec{e}_y \quad (3.2)$$

The Quadruple trap offers the best confinement, but suffer from a critical loss called Majorana loss [31, 32, 33, 34] which prevents it from being the trap to BEC. The Majorana loss is caused by a spin flip near the zero crossing of the magnetic field, the spin flip occurs

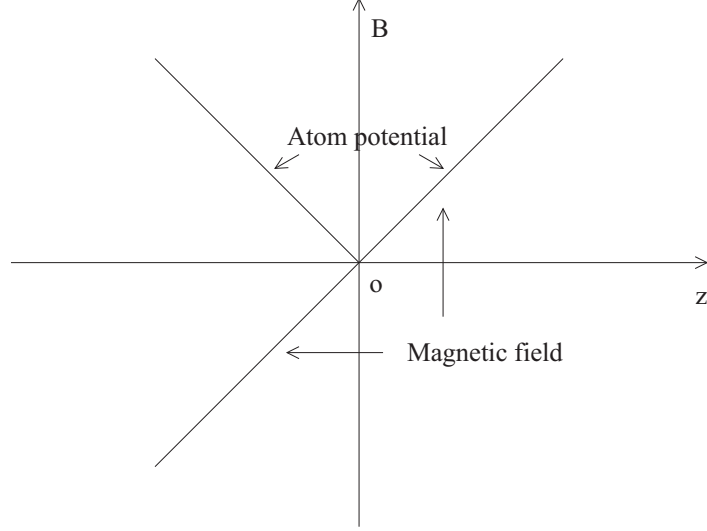


Figure 3.2: Spherical Quadruple Trap Field and Potential

due to the violation of the adiabatic condition that requires the Larmor frequency to be larger than the angular frequency at which the moving atoms perceive a rotating magnetic field. The hole of Majorana loss has a size of about $\sqrt{2\hbar v/\pi\mu B'}$.

In order to eliminate the Majorana loss, different magnetic traps are invented, and I will introduce them in the following sections.

3.2 TOP Trap

The time-averaged, orbiting potential trap (TOP) [35] is formed by adding a rotating magnetic field to the Quadruple trap, as shown in Fig. 3.3. The rotating field shifts the instantaneous center of Quadruple field away from the center of the trap. The rotating frequency is much higher than the orbiting frequency of the atoms, but much lower than the Larmor frequency. The atom spin will still follow the local B field, but they feel a time averaging potential of the total field.

Since the rotating field is on the radial plane, from Eq. 3.2, we have

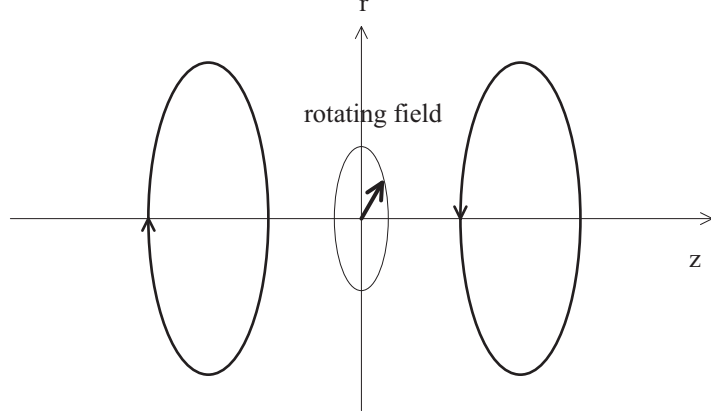


Figure 3.3: TOP

$$|\vec{B}|^2 = |B_z \vec{e}_z + B_r \vec{e}_r + \vec{B}_T|^2 = B_z^2 + B_r^2 + B_T^2 + 2B_r B_T \cos\theta \quad (3.3)$$

where θ is the angle between \vec{B}_r and \vec{B}_T .

On the z axis, $B_r = 0$, we have

$$|\vec{B}|^2 = B_z^2 + B_T^2 \quad (3.4)$$

$$|\vec{B}| = \sqrt{B_z^2 + B_T^2} = \sqrt{(B'_z z)^2 + B_T^2} \simeq B_T + \frac{1}{2} \frac{B_z'^2}{B_T} z^2 \quad (3.5)$$

So the trap is of a harmonic shape and the axial curvature is

$$B_z'' = \omega_z^2 = \frac{B_z'^2}{B_T} \quad (3.6)$$

On the radial direction, $B_z = 0$. When $B_r \ll B_T$, from Eq. 3.3, and expanding it to the second order of $\frac{B_r}{B_T}$, we have

$$|\vec{B}| = \sqrt{B_r^2 + B_T^2 + 2B_r B_T \cos\theta} \simeq B_T \left[1 + \frac{1}{2} \left(\frac{B_r}{B_T} \right)^2 + \frac{B_r}{B_T} \cos\theta - \frac{1}{2} \left(\frac{B_r}{B_T} \right)^2 \cos^2\theta \right] \quad (3.7)$$

Considering that the time average of $\cos\theta$ and $\cos 2\theta$ is zero, we have

$$|\vec{B}| \simeq B_T \left[1 + \frac{1}{2} \left(\frac{B_r}{B_T} \right)^2 + 0 - \frac{1}{4} \left(\frac{B_r}{B_T} \right)^2 \right] = B_T \left[1 + \frac{1}{4} \left(\frac{B_r}{B_T} \right)^2 \right] \quad (3.8)$$

So, there is a harmonic potential in the radial direction too, and we have

$$B_x'' = \omega_x^2 = \frac{B_x'^2}{2B_T} = \omega_z^2/8 \quad (3.9)$$

and

$$B_y'' = \omega_y^2 = \frac{B_y'^2}{2B_T} = \omega_z^2/8 \quad (3.10)$$

On the $z = 0$ plane, there is a circle made of the instantaneous magnetic field zero. If an atom can reach this circle, it will go through a Majorana loss and be ejected from the trap, so this circle is called circle of death. The size of the circle, which decides the size of the trap, is given by

$$R_{TOP} = B_T/B_r' \quad (3.11)$$

The trap depth of the TOP trap is decided by the potential difference of the circle of death and the center of the trap. At the trap center, the average B field is B_T , and at the circle of death, the average B field, taken from Eq. 3.3 and considering $B_r = B_T$ at the circle of death, we have

$$|\vec{B}| = \sqrt{B_r^2 + B_T^2 + 2B_r B_T \cos\theta} = \sqrt{2B_T^2 + 2B_T^2 \cos\theta} = 2B_T \cos \frac{\theta}{2} \quad (3.12)$$

The average of θ over 2π gives us

$$B_{circle} = \frac{4B_T}{\pi} \quad (3.13)$$

so the trap depth is

$$U_{depth} = \frac{4B_T}{\pi} - B_T \simeq \frac{1}{4}B_T \quad (3.14)$$

The TOP trap fixed the Majorana hole in the Quadruple trap, but it has many serious disadvantages. First, the trap depth, given by Eq. 3.14, is relatively shallow. A typical TOP trap can generate 100G of rotating field. This indicate a 25G trap depth, enough for Rb and Na, which can be perfectly cooled by Sub-Doppler cooling. For Li, the Sub-Doppler cooling does not work; the typical temperature in the MOT is about $500\mu K$, and the transfer efficiency to the TOP is inefficient. Secondly, at the maximum trap depth, the curvature or the confinement of the trap, given by Eq. 3.6, Eq. 3.9, and Eq. 3.10, is badly hurt. This trade-off of TOP trap at a deep trap depth makes it even worse for deep traps. Lastly, the instantaneous variation of the magnetic field in the TOP is 8 times larger compared to other DC magnetic traps, and this made it inappropriate for some tricks, such as Doppler cooling inside the trap.

3.3 Ioffe-Pritchard Trap

The Ioffe-Pritchard trap is one of the most successful traps used to achieve BEC [36, 37, 38]. There are many different implementations of this trap [40, 41, 42], but we will illustrate the characteristics of the Ioffe-Pritchard trap with the standard configuration of the trap.

As shown in Fig. 3.4, the standard configuration of the Ioffe-Pritchard trap consists of 4 Ioffe bars which generates the 2-D Quadruple field, and a pair of pinch coils that provide confinement in the axial direction.

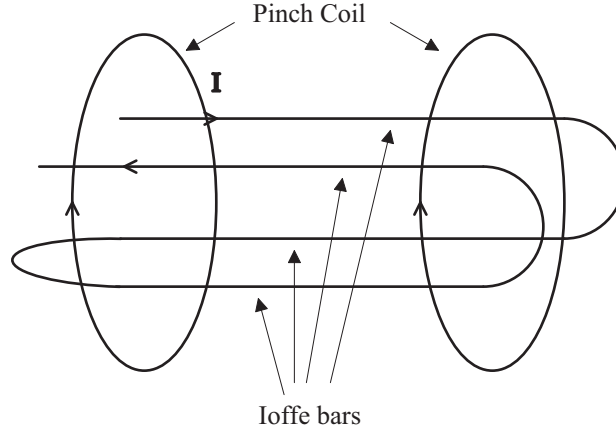


Figure 3.4: A Typical Ioffe-Pritchard Trap

The Ioffe-Pritchard trap magnetic field is the sum of the field from the Ioffe bar \vec{B}_I and the pinch coil \vec{B}_P

$$\vec{B}_{IP} = \vec{B}_I + \vec{B}_P \quad (3.15)$$

For an axial symmetric Ioffe-Pritchard trap in cylindrical coordinates [39],

$$\vec{B}_I(\rho, \phi, z) = B'_r \rho \cos 2\phi \hat{\rho} - B'_r \rho \sin 2\phi \hat{\phi} \quad (3.16)$$

$$\vec{B}_P(\rho, \phi, z) = -\frac{B''_z}{2} \phi z \hat{\rho} + [B_0 + \frac{B''_z}{2}(z^2 - \frac{\rho^2}{2})] \hat{z} \quad (3.17)$$

If we combine the above 2 equations, and the magnitude of the B field is

$$|\vec{B}_{IP}| = B_0 \sqrt{1 + [(\frac{B'_r}{B_0})^2 - \frac{B''_z}{2B_0}] \rho^2 + \frac{B''_z}{B_0} z^2 - \frac{B'_r B''_z}{B_0^2} \rho^2 z \cos 2\phi + (\frac{B''_z}{2B_0})^2 (z^4 + \frac{\rho^4}{4})} \quad (3.18)$$

From Eq. 3.18 , the potential close to the center can be approximated to the second order, as the anisotropic harmonic oscillator:

$$U_{IP}(\rho, z) = \frac{\mu}{2}(B_r''\rho^2 + B_z''z^2) \quad (3.19)$$

in which

$$B_r'' = \frac{(B_r')^2}{B_0} - \frac{B_z''}{2} \quad (3.20)$$

Typically, $\frac{(B_r')^2}{B_0} \gg \frac{B_z''}{2}$, so that the radial curvature is $\frac{(B_r')^2}{B_0}$. The bias field B_0 only needs to be large enough to avoid Majorana loss, and can be set lower than 1G. This is much better than the TOP, where B_T has to be large enough to maintain a decent trap depth.

Ioffe-Pritchard trap has been realized in many different variations, including the "clover-leaf" configuration, the "QUIC" trap, or a 4D coil trap. Among these different traps, the "QUIC" trap has a great advantage in that it does not require the precise alignment of the trap center to the center of the MOT. The atoms are transferred first into a Quadruple trap, which uses the same set of coils as the MOT coil, and it is thus easy to align, and when they adiabatically turn on the 3rd mall coil, the Quadruple trap smoothly changes into a Ioffe-Pritchard trap, avoiding unnecessary heating.

3.4 Scaling Law

When designing a magnetic trap, it is important to keep in mind the scaling law. With the same current, the trap depth scales inversely with the trap size, the gradient scales inversely with the size square, and the curvature scales inversely with the size to the third. Therefore, a small trap is favorable over a big trap. However, this consideration is over simplified because it assumes that the current in the coil does not change. Obviously, this is not true in real experiments. A big coil conducts a much bigger current than a small coil. If we were to assume that a big trap maintains the same current density as a small

trap, the current of the big trap will scale with the square of the size, so the trap depth will scale linearly with the trap size, and the trap gradient maintains the same with different trap size. For a Ioffe-Pritchard trap, the radial curvature did not change with the different trap size, the axial curvature scales linearly with the trap size. This scaling law looks much worse than the previous scaling.

So, what really stands behind a small coil? There are several answers to this question, and the first is that if the current density is maintained, the total power dissipation will scale to a third of the size, and this easily puts a big coil at a serious disadvantage. They usually dissipate KW and above, they are hard to power, and hard to switch, while a small coil, such as the Mini-Trap we designed, is very easy to switch on and off due to its small self-inductance and cooling, owing to the small power dissipation at 7W. The second is that it is hard for a big trap to maintain the same current density as a small trap; the heat that a big trap generates has to go travel a longer distance to dissipate into the heat sink. A simple 1-D model shows that with the same current density, the temperature rises in the center of the trap scales as the size squares, so the current density of big traps are much smaller than the density of a small trap. Big traps use water cooling through the hollow copper wire; the hole in the middle of the wire sacrifices the current conducting area of the wire and makes it hard to increase the average current density. The last is that with a small trap, due to the minimum power dissipation, they can be put in a liquid nitrogen cold finger, and under this temperature, the electrical conductivity of copper increases by a factor of 8, and the thermal conductivity of alumina increases by a factor of 3, making it possible for a small trap to further increase the current density. With modest cooling, our Mini-Trap reaches a current density of $35A/mm^2$ in the Ioffe bar and $200A/mm^2$ in the pinch coil before it affects the trap lifetime, and it is bigger than the current density of our previous heavily water-cooled big coil at $25A/mm^2$.

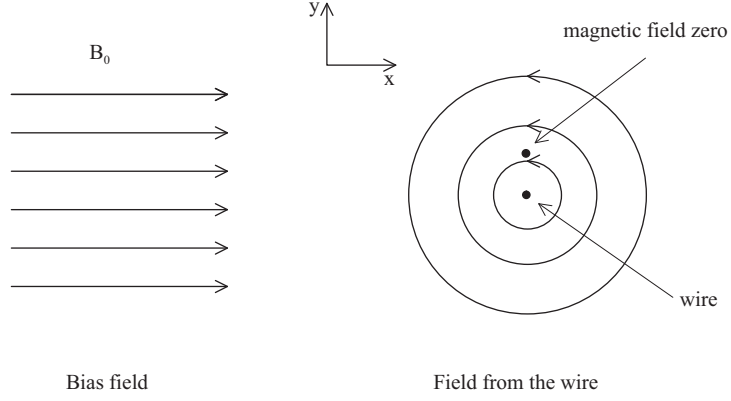


Figure 3.5: 2-D Micro-Trap

3.5 Micro Traps

A Micro Trap is a trap made of microscopic lithographic conductors on a chip. The size of the conductor can be as small as a few microns, and the size of the trapping volume is on the same order of magnitude. The substrate of the chip is usually made of good thermal conductors such as alumina (Al_2O_3 ceramic), and heat generated in the wire can be easily dissipated into the substrate so the current density in the wires can be several orders of magnitude greater, up to $10^5 A/mm^2$. A typical micro trap design is shown in Fig. 3.5.

The trap is comprised of a current-carrying thin wire and a uniform bias field that is perpendicular to the wire. When the field generated by the thin wire has the same amplitude and is in the opposite direction of the uniform bias field, there is a magnetic field zero, which leads to a local magnetic field amplitude minimum and forms a nice 2-D Quadruple trap. The radial field is shown in Fig. 3.6.

In order to provide the confinement in the axial direction, either a “Z” shaped or a “II” shaped wire is used. Both of them use the middle segment and the bias field to provide the 2-D Quadruple trap in the radial direction and use the end segments to provide the axial confinement. For the “II” shaped wire, the two end segments cancel each other at the center of the trap, so it forms a Quadruple trap and suffers from the Majorana loss.

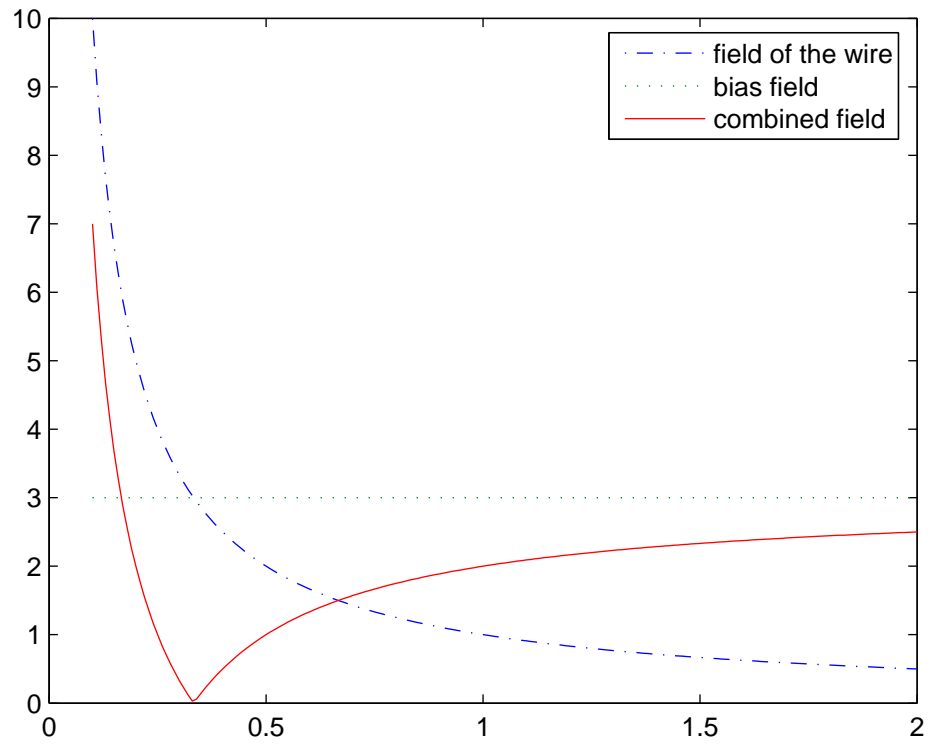


Figure 3.6: 2-D Micro-Trap Field in the Radial Direction

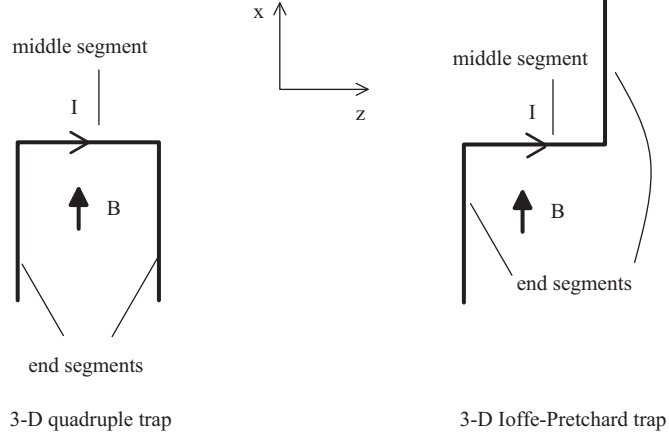


Figure 3.7: 3-D Micro-Trap

For the “Z” shaped wire, the two end segments give a small field along the axial direction in the middle of the trap, thus it forms an Ioffe-Pritchard trap. This is the trap people used to get the BEC. The configuration of the 3-D Micro-Trap is shown in Fig. 3.7 and the field of the “Z” and “ Π ” shaped trap are shown in Fig. 3.8.

3.6 Lithium Elastic Collision Cross-Section

The advantage of the Micro-Trap is its huge trap gradient and curvature. Due to the fact that the trap is very small and the current density is very high, in such a tight trap, after adiabatic compression, the elastic collision rate increases significantly. As a result, Rb BEC has been achieved within a few seconds [55, 56].

However, this does not work well with Lithium. The problem lies in the fact that, the elastic collision cross-section of Lithium drops with increased temperature [57]. The $|F = 2, m_F = 2\rangle$ state has a negative scattering length, so as the collision energy increases, the collision cross-section drops, and it goes down to zero at $8mK$. The average collision cross-section drops significantly as the temperature increases. This canceled most of the advantages gained from adiabatic compression. This problem does not occur for Rb and N_a .

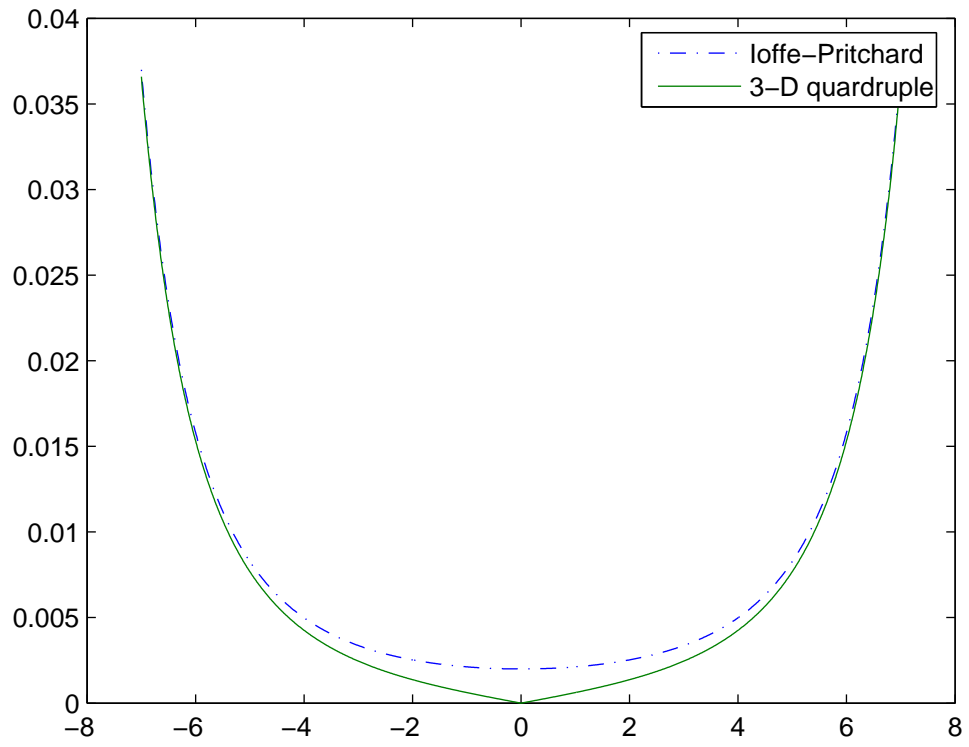


Figure 3.8: 3-D Micro-Trap Axial Field

The trapping volume of the Micro-Trap is much smaller than the size of a typical MOT, and it is hard to transfer enough atoms into the Micro-Trap, a typical number of atoms that can be loaded into the Micro-Trap is around 10^6 , which is 2 orders of magnitude smaller than the number loaded into a traditional trap. In the Rb BEC experiment with Micro-Traps, due to the huge confinement, the atoms can be adiabatically compressed to make them much denser and with a significant increase in the temperature, both of these increase the elastic collision rate. The disadvantage of a smaller number of trapped atoms is compensated for, but for Li, the elastic collision cross-section drops with high temperatures, and adiabatic compression does not work as well as for Rb. Until today, there have been a couple of Rb BEC with Micro-Trap in the world, yet no one has achieved Li BEC with Micro-Trap.

3.7 The Mini-Trap

In order to build a trap small enough to have a low level of power dissipation, good confinement, and a decent trap depth, while at the same time maintaining a big trapping volume to load enough atoms in the trap, we designed the Mini-Trap.

The Mini-Trap is a typical Ioffe-Pritchard trap, as shown in Fig. 3.9. It is made of four pieces. The first piece is machined from a piece of oxygen free copper, which is made up the four Ioffe bars and a pinch coil. The outer diameter is 8mm and the inner diameter is 5mm. The second piece is made of a ceramic chip which has the connection trace connected to the incoming and outgoing current lead and another circle to make the other pinch coil. The third piece is a copper tube that supplies the incoming current and water cooling to the Mini-Trap. The fourth piece is a copper tube that functions as an outgoing current lead for the Mini-Trap. The four pieces are welded together to create a robust current, thermal conduction, and good vacuum property.

Due to its planar geometry, the Micro-Trap sacrifices both in the radial and axial

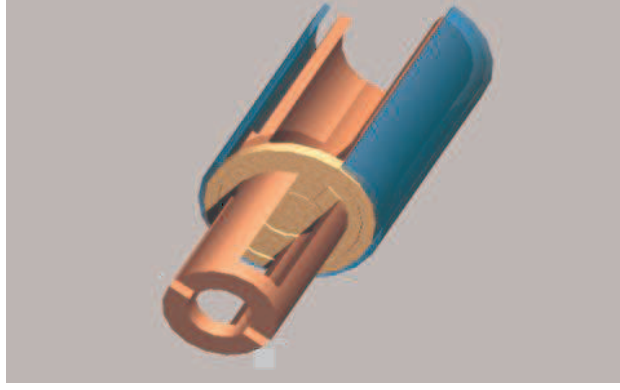


Figure 3.9: minitraps

confinement. In the radial direction, there is only one wire to supply the radial confinement, and this reduces the radial gradient by a factor of 4. In the axial direction, both the “ Z ” shaped and the “ Π ” shaped trap gives a factor of 2π smaller field compared to a ring. The advantage of the Micro-Trap design is that by increasing the bias field, the trap moves closer to the wire and the trap becomes smaller and tighter, which cannot be performed with the Mini-Trap.

The size of the Mini-Trap is similar to the size of the MOT. This makes it much easier to transfer a lot of atoms to the Mini-Trap. Compared to the traditional big traps, Mini-Trap dissipates less than 10W at 100A, has a 100G trap depth, and compares favorably to the big traps in field gradient and curvature.

3.8 Transferring Atoms to the Magnetic Trap

It is very important to transfer the atoms in the MOT to the magnetic trap with a minimum loss of phase space density. This requires both mode matching between the MOT and the magnetic trap, and the precise alignment of the center between the MOT and the magnetic trap. Mode matching is easy to achieve because both the Quadruple trap and the Ioffe-Pritchard trap can operate in a similar aspect ratio and confinement comparable

to the MOT. Some traps have a totally different aspect ratio from the MOT; a tight Ioffe-Pritchard trap usually is cigar-shaped, and in this case, the atoms can be transferred into an Ioffe-Pritchard trap with the similar aspect ratio to the MOT first, and then the trap can be (for example, by lower the bias field in the trap center) adiabatically deformed into the final shape. However, the adiabatic process cannot be performed between a Quadruple trap and an Ioffe-Pritchard trap. Due to their topological difference, a smooth transform from a Quadruple trap to an Ioffe-Pritchard trap will cause a potential hole in the trap.

The alignment of the center of the traps is a different story. For Quadruple traps, it is easy to align the center of the MOT to that of the Quadruple trap. Many experiments use Quadruple trap coils at a lower current to provide the field gradient for the MOT, in this case, just make sure the background stray field is properly compensated, and this will guarantee that the center of the 2 traps are aligned. For the Ioffe-Pritchard trap, the center of the magnetic trap really depends on its alignment because there is no simple way to align the center of the magnetic trap to the center of the MOT.

A very smart idea is presented by T. Esslinger et al. [46], as shown in Fig. 3.10. They first transferred the atoms to a Quadruple trap, then smoothly turned on the Ioffe coil. An easy way to understand how it works is as follows. In the radial direction of the Quadruple coil, the Ioffe coil generates a field in the reverse direction of the Quadruple coil, and this changes the saddle point in the radial direction into a potential minimum, although the field from the Ioffe coil is not uniform and will change the position of the saddle point. The real magnetic field plot is shown in Fig. 3.11.

When the Ioffe coil is off, it is a typical Quadruple field. When the current in the Ioffe coil starts to ramp and we see that the saddle point is closer to the center of the Quadruple trap and we see the emergence of a second field zero in addition to the original field zero of the Quadruple field. When the current in the Ioffe coil is getting bigger, and the two field zero is getting closer, and finally, the current in the Ioffe coil is ramped to the final value and the two field zero merges. With a further increase in the current in the Ioffe coil, the

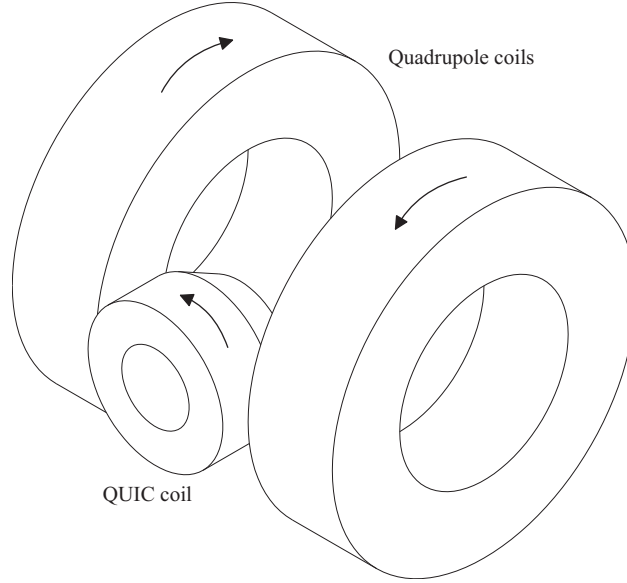


Figure 3.10: The QUIC Trap Geometry

field minimum will rise a little above zero to avoid the Majorana loss, and this will result in a nice Ioffe-Pritchard trap.

The process of the two field zero merge is not an adiabatic process because if the current in the Ioffe coil ramp backs down, the zeroes will split and the atoms will stay in both zeros, which is different from the initial situation where all the atoms stay only in one zero. So the process is not reversible, hence not adiabatic. However, the process is a smooth process. It does not require any alignment and has a minimum loss of phase space density.

3.9 Semi-Adiabatic Transfer to the Mini-Trap

We could use the transfer scheme that was introduced in the previous section. However, due to the geometry limits in our chamber, we were not able to, so instead, we invented another transfer scheme, as shown in Fig. ??.

The atoms are first transferred into the Quadruple trap formed by the MOT coils. Then the current in the MOT coil is adiabatically ramped down and the current in the lower

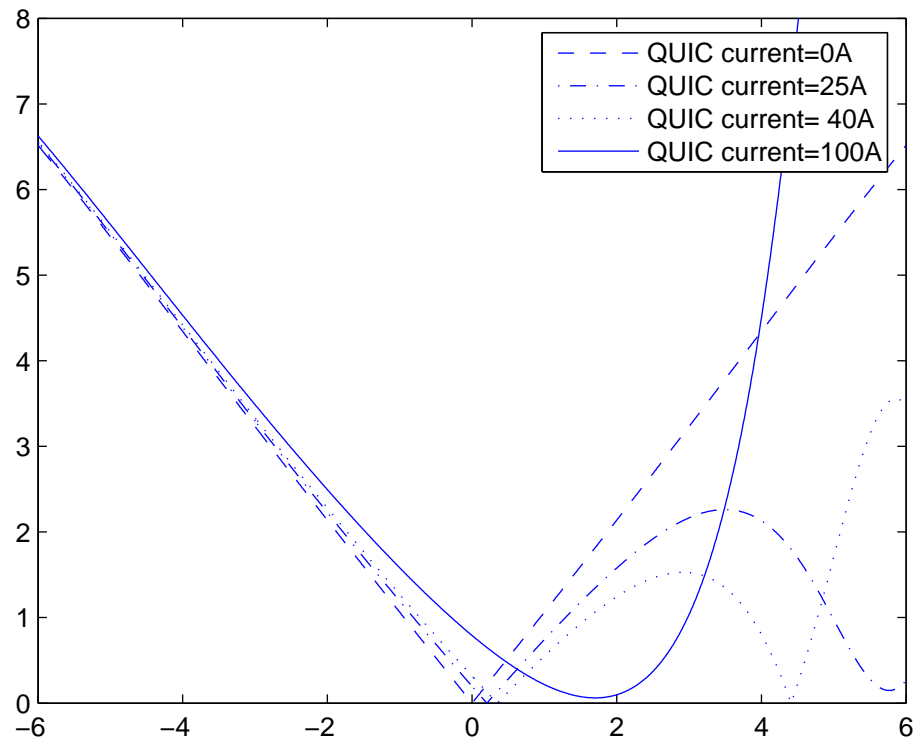


Figure 3.11: The QUIC Trap Field Plot

set of rectangular coils are ramped up. The atoms are adiabatically transferred into the Quadruple trap by the lower Quadruple trap, and now the cloud looks like a cigar, with an aspect ratio that is similar to the Mini-Trap. The cloud is then lifted up by ramping down the lower set of Quadruple coils and ramping up the upper set of Quadruple coils. Now the cloud is in the center of the Mini-Trap.

The cloud is still in a Quadruple trap, which is not topologically compatible with the Mini-Trap, so we cannot do a adiabatic transfer to the Mini-Trap. However, we found that the oscillation frequency in the radial direction is much bigger than the axial direction. If we ramp the current in a time scale that allows the atoms to go through several radial oscillations but have no significant motion in the axial direction, we can achieve an adiabatic transfer in the radial direction. The alignment only needs to be perfect in the axial direction, which is much easier because the axial cloud size is much bigger than the radial size.

It turns out that this transfer scheme works very well. We tried to reverse the current direction in the elevator coil to break the semi-adiabatic transfer but found that the transfer efficiency is much worse and all the atoms were lost in 2 seconds, indicating a huge heating process during the transfer.

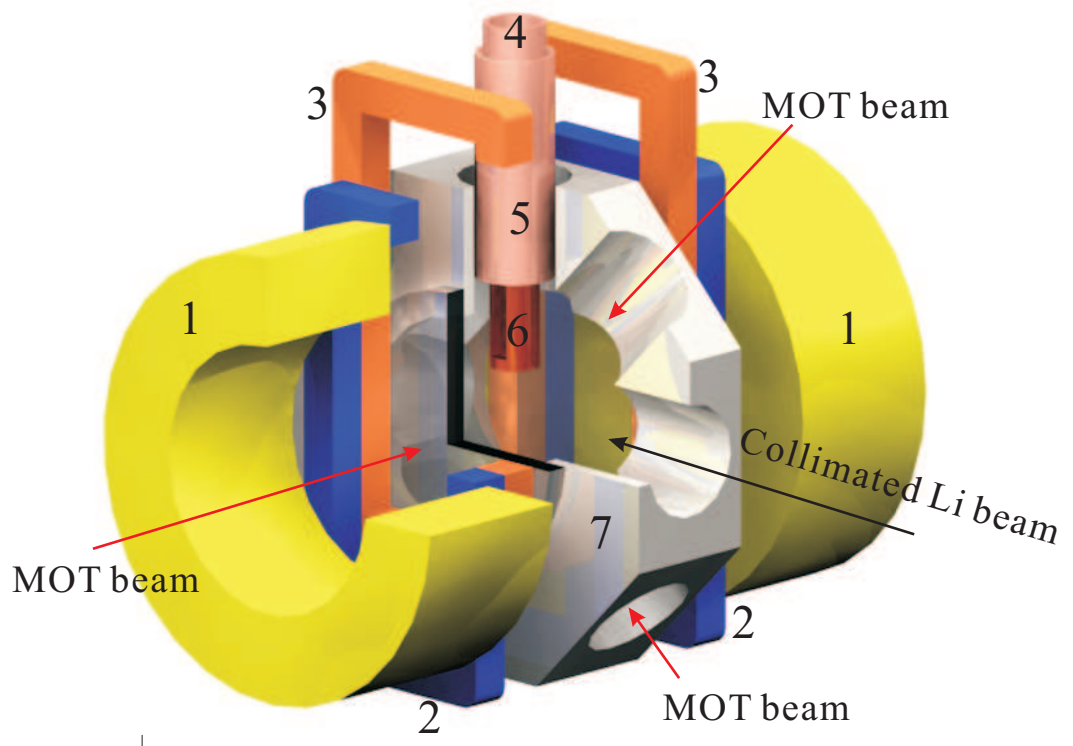


Figure 3.12: The trap setup. 1.MOT coils 2.Lower rectangular coils 3.Upper rectangular coils 4.The negative lead of the Mini-Trap 5.The positive lead of the Mini-Trap 6.Mini-Trap 7.Vacuum chamber

Chapter 4

Evaporative Cooling

Evaporative cooling is the most efficient technique to cool atoms at an extremely low temperature and high density. The principle for evaporative cooling is very simple. There are always high energy particles in the tail of the Maxwell-Boltzmann distribution, and in the evaporative cooling process, these high energy particles are selectively removed, so the average energy of the remaining atoms are lower. After a while, the remaining atoms will reach thermal equilibrium again through elastic collisions. The remaining gas, with a lower average energy, has a lower temperature than the initial gas. Evaporative cooling not only reduces the temperature of the atoms, but also increases the phase space density of the atoms. During the re-thermalization process, when two atoms elastically collide, they can generate a high energy atom which is removed from the cloud through evaporative cooling and one low energy atom that stays in the trap; this process increases the phase space density at the energy of the low energy atom. If the collision generates 2 atoms whose energies are both below the evaporative cooling threshold, the phase space distribution does not change due to the detailed balance.

Evaporative cooling happens on an exponential scale [43, 44]; the number of atoms, temperature, and density all change with the exponential of the time. A typical evaporative cooling process often controls the depth of the potential to the ηKT ; when η is big, the

average energy taken away by the ejected atoms is higher so the cooling efficiency is higher as well, but a bigger η also makes the evaporative cooling slower, which causes a bigger loss from background loss and inelastic loss. The optimal cooling is to choose a η that results in a good trade off between these two factors.

In order to maintain sustained evaporative cooling, we need to maintain or increase the elastic collision rate $nv\sigma$, where n is the density of the atoms, v is the speed of the atoms, and σ is scattering cross-section of two atoms. If the the elastic collision rate decreases, the re-thermalization time will increase exponentially and stop the evaporative cooling very quickly. The main figure of merit is the ratio between the elastic collision rate and the background gas collisions $R = \tau_{loss}/\tau_{el}$. The theory shows that for an optimized η , a linear trap requires a $R > 150$ and a harmonic trap requires a $R > 400$ [43, 45]. This is the most important threshold condition that determines if an evaporative cooling sequence can lead to a BEC.

Chapter 5

Experimental Setup

5.1 Overview

The experiment is similar to other BEC experiments. A Lithium oven generates the Lithium atomic beam source and this is transversely cooled by two pairs of zigzag broad-band laser beams. The collimated atom beams go through a differential pumping tube and enter the main chamber, where they are slowed and captured by a broad-band MOT. After the MOT is fully loaded, the atoms are cooled by Doppler cooling, pumped to the $|F = 2, m_f = 2\rangle$ state, and trapped by the Quadruple trap. The atoms are raised to the center of the Mini-Trap by the 2 sets of rectangular Quadruple coils and semi-adiabatically transferred to the Mini-Trap. Then the atoms are evaporative cooled by RF induced cooling.

5.2 Lithium Energy Level Scheme and Laser Setup

The Lithium energy scheme is shown in Fig. 5.1. The cooling transition is from the $2S_{1/2}$ $|F = 2\rangle$ ground state to the $2P_{3/2}$ $|F' = 3\rangle$ excited state. An excited state atom has a certain probability to spontaneously decay to the $|F = 1\rangle$ ground state, and since there is no light interacting with the $|F = 1\rangle$ state, they are called the dark state. In a

real MOT, this process will quickly pump all the atoms into the dark state. Atoms in the dark state stop interacting with the light and are lost from the MOT. The time scale of the pumping is in the μs scale.

To fix this problem, a so-called repumping light from the $|F = 1 >$ to the excited state is brought in to bring the dark state atoms back to the cycle.

After the MOT loading and cooling stage, the atoms are optically pumped into the $|F = 2, m_f = 2 >$ state and trapped in the magnetic trap. The optical pumping happens in two steps. In the first step, only the repumping light is on, and all the atoms are pumped into the $|F = 2 >$ state. In the second step, a bias field of 10G and a σ^+ light that resonates with the $2S_{1/2} |F = 2 >$ to the $2P_{1/2} |F' = 2 >$ transition are turned on. According to the conservation of angular momentum, the light will always bring atoms from the $|F = 2, m_f >$ state to the $|F' = 2, m'_f + 1 >$ state. The atom then spontaneously decays to the ground state. If atoms decay to the $|F = 2, m_f = 2 >$ state, they will stop interacting with the pumping light, so $|F = 2, m_f = 2 >$ is a dark state. After several cycles, all the atoms are pumped to the $|F = 2, m_f = 2 >$ state, which is the state that we want to trap.

The laser setup is shown in Fig. 5.2, in which a coherent 899 dye laser gives an output of about 700mW, the dye laser is locked by saturation spectroscopy [58] to 75Mhz below the $|F = 2, m_f = 2 >$ to the $|F' = 3, m'_f = 3 >$ transition. The output light of the dye laser go through a 200Mhz AOM, and if the AOM is turned on, some light will be deflected into the +1 order and double pass the AOM. After that, this light goes through another 200Mhz double pass AOM, and the frequency is shifted about 800Mhz higher and becomes resonant with the $|F = 1 >$ to $|F' = 2 >$ transition. We use this light, which only interacts the $|F = 1 >$ ground state to the excited state, to pump all the atoms into the other $|F = 2 >$ hyperfine ground states. During the loading and cooling, the 200M AOM is turned off. The laser will pass it without being deflected and it will pass a 800Mhz EOM. This EOM brings 1/5 of the total optical power into the ± 1 order. The +1 order

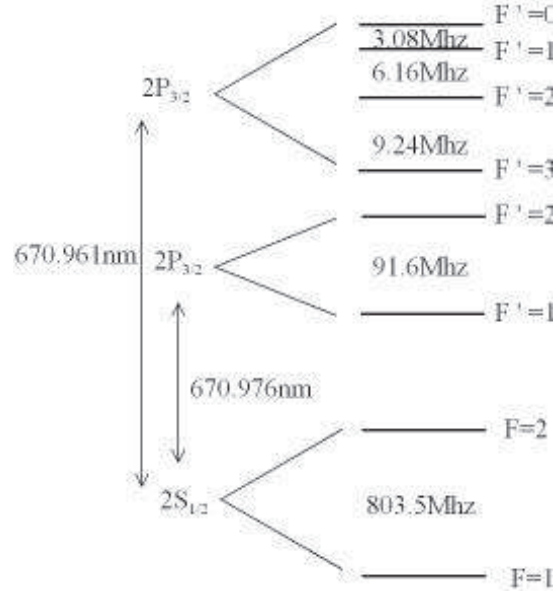


Figure 5.1: Lithium Energy Level Scheme

is resonant with the $|F = 1 \rangle$ to $|F' = 2 \rangle$ transition and is used as the repumping light. After the 800Mhz EOM, the light goes through a 75M AOM that works as a fast switch. If it is on, the light is deflected and goes through a 75M AOM double pass. The final frequency is roughly on a resonance with the $|F = 2, m_f = 2 \rangle$ to $|F' = 3, m'_f = 3 \rangle$ transition, and this beam is used as the Doppler cooling beam. If the AOM is off, the light, which remains at 75Mhz below the $|F = 2, m_f = 2 \rangle$ to $|F' = 3, m'_f = 3 \rangle$ transition, goes through a double pass 11.9Mhz EOM. This EOM is heavily modulated and generates a frequency comb that covers the frequency band from 0 to 150Mhz below the $|F = 2, m_f = 2 \rangle$ to $|F' = 3, m'_f = 3 \rangle$ transition. The separation of the teeth of the comb is 11.9Mhz, roughly twice the natural line width of the $|F = 2, m_f = 2 \rangle$ to $|F' = 3, m'_f = 3 \rangle$ transition. The light intensity is strong enough for all the teeth to saturate the transition, so this light acts as a 150M continuous spectrum. This broad-band light is used during the loading of the MOT as the MOT beam and the transverse cooling beam.

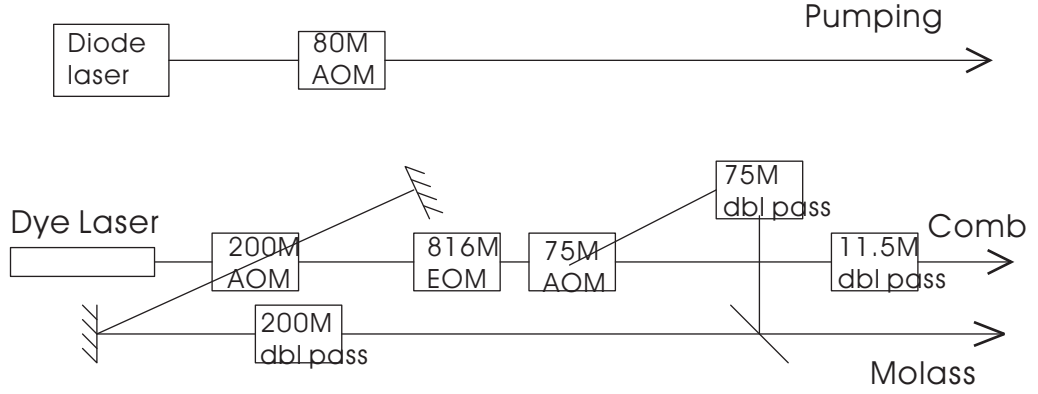


Figure 5.2: Laser Setup

5.3 Construction of an Extended Cavity Diode Laser

A home-made extended cavity diode laser with an output of 10mW is locked to the $|F = 2, m_f = 2\rangle$ to $|F' = 2, m'_f = 2\rangle$ transition, and this light is used as the Zeeman pumping light. We basically follow the design of A.S. Arnold et al. and Hawthorn et al. [47, 48]. Compared with the popular design from Ricci et al. [49], It is easy to build, and because the grating mount is a commercial precision mirror mount, it can be tweaked for years without becoming loose and hysteretic. The disadvantage is that the mirror mount is a poor thermal conductor, so the thermal drift of the cavity length is bigger. Also, the springs in the mirror mount have resonant frequencies and are easy to couple to the vibrations from the environment. These disadvantages are less harmful to our experiment because optical pumping is less sensitive to laser jitter and drift.

With respect to the electronics parts, we designed a logic circuit that automatically locks the laser when the dispersion range falls in the lock range specified by 2 timing edges; this makes the locking of the laser a snap, and we usually spend less than 10 seconds to lock the laser. We also use a novel 2 Piezo control, one for scanning and another for locking. The scanning Piezo is a highly sensitive Piezo stack with broad scanning range. Because It is not in the servo loop, there is no band-width requirement for the driver. Its driving

circuit is heavily filtered by big capacitors. This makes it possible for a super low noise Piezo driver. The advantage is significantly reduced noise on the Piezo, which is important for highly sensitive Piezo. We also use a switch to connect a battery to the output of the Piezo driver to further increase the scan range. Because the battery does not have DC current output from the Piezo, it has very long life span; our 9V battery pack has been working for over one year. The lock Piezo is a low sensitive Piezo pack which has a much smaller scanning range (about 300Mhz). Because of its smaller scanning range, the Piezo stack is very thin. This makes it possible for it to work in a high frequency. It is much less sensitive to driver noise, so we can use a broadband driver to improve servo response speed. Both Piezo drivers only need 30V output and can be built from a simple OP-amp.

A good homepage at <http://optics.ph.unimelb.edu.au/atomopt/diodes.html> describes the design of the laser. The geometry is the same as the Fig.1 from reference [48]. However, in our design, we put the Peltier cooler at the back of the laser diode assembly and surrounded it with a thick aluminum block. This guaranteed a perfect temperature control for the laser diode. We use a Optometrics LLC (catalog No. 3-4182) diffraction grating. We found that even without gold coating, the grating still works fine. The laser diode is a HL6714G ordered from Thorlabs with a 10mW output power, at our wave length of 670um, its output is pretty high. For R_b wavelength at 780um, It is easy to get a diode of much higher output power of 100-200mW. As described in reference [48], a Newport U100-P precision mirror mount was modified to be the grating mount. The screw that adjusts the grating incoming angle was replaced with the scanning Piezo stack. Another home-made lock Piezo stack was glued under the grating to lock the laser. We made the Piezo stack from Piezoelectric single sheet ordered from Piezo System, Inc. (www.piezo.com) part No. T110-A4E-602. Four Piezo squares of 15mm x 15mm were cut from the sheet. The sheet is pretty thin and can be easily cut with a razor blade. The Piezo has a positive side and a negative side, which have to be connected to a positive and negative voltage respectively, a mistake can destroy the Piezo sheet. A soft and thin copper sheet is glued to the surface

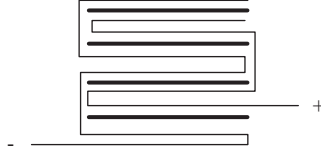


Figure 5.3: A Home-made Piezo Stack

of the Piezo sheets to become the electrical lead, as shown in Fig. 5.3

The Peltier cooler is a Marlow Industries, Inc. DT3-6 Peltier cooler, with a maximum voltage of 3.6V and maximum current 5.6A. We use a Wavelength Electronics Inc. TEC-2000 temperature controller to stabilize the temperature of the laser diode. The power supply for the TEC-2000 is from a used PC AT power supply, which can easily output 5A at +12V and 10A at +5V; there is also -12v and -5V output of a few hundred mA for the control electronics. The temperature sensor is a 10K thermistor. We also have a AD590 temperature sensor to monitor the temperature.

The current controller was copied from Libbrecht et al. [50]. The controller uses an extremely low noise OP-amp LT1028 and a temperature-regulated precision voltage source to form a high precision, highly temperature stable and low noise current source. The current controller also has soft start and plenty of current modulation options. The only disadvantage is by using a single end output, the output impedance is not low enough, and this can cause a big phase lag when driving a high capacitive load such as a high power laser diode. For our diode system, we do not have a feed back loop for the current, this controller would be overkill. The current controller tends to oscillate if the pole canceling RC serial branch does not match the second pole frequency. The branch is connected to the gate of the output transistor, and it is easy to find the a stable point by varying the resistor.

The scanning ramp generator, PI controller, and the Piezo driver are home design versions. One problem with the Piezo driver is the trade off between the scan range and the noise. A typical Piezo driver is a 10x high voltage amplifier with a output range of

150V or more, and this amplifier is very easy to couple to input noise. A high voltage amplifier is also hard to build in order to achieve fast response. In our design, we solve this problem by using 2 Piezos. The first Piezo stack is used to have broad scan range. It is not involved in the servo. We can easily bypass the noise with a good low pass filter.

When we scanned the laser, the dispersion line was very easy to see. In the usual design, we would have had to decrease the scan range to half a line width to lock the laser. In our design, we made it possible to have a big scan range, which not only made it easier to adjust, but also less likely to lock to the wrong dispersion signal. In the circuit, we used the scan generator's integrator as the locking feed-back controller's integrator. When we switched the scan mode to the lock mode, the capacitor's voltage was sitting exactly in the appropriate slope of the dispersion line.

The automatic switch was done by a simple logic circuit. Two "one shots" (74LS123) defined the enable timing window, a comparator (LM393) found the zero crossing point, and a D flip-flop (74LS74) settled down the transition from scan mode to lock mode. The corresponding signal switch was done by a MOSFET switch.

So when we used it, we first find the dispersion signal, then adjust the time window to the zero crossing we want, and turn on the switch to tell the automatic lock circuit to be ready, and this way, the next time the scan goes through the zero crossing, the lock circuit kicks in and the laser is locked.

5.4 Vacuum Design

The vacuum chamber is divided into 3 parts, as shown in Fig. 5.4. The left chamber contains the Lithium source. Lithium has a melting point of 180.54°C , so we have to heat the Lithium oven up to 290°C to achieve the appropriate Lithium atom flux. The vacuum level of this chamber cannot be very high because the terrible outgassing from the Lithium oven. We maintain a pressure of roughly 10^{-9} Torr with a 30l/s diode ion pump.

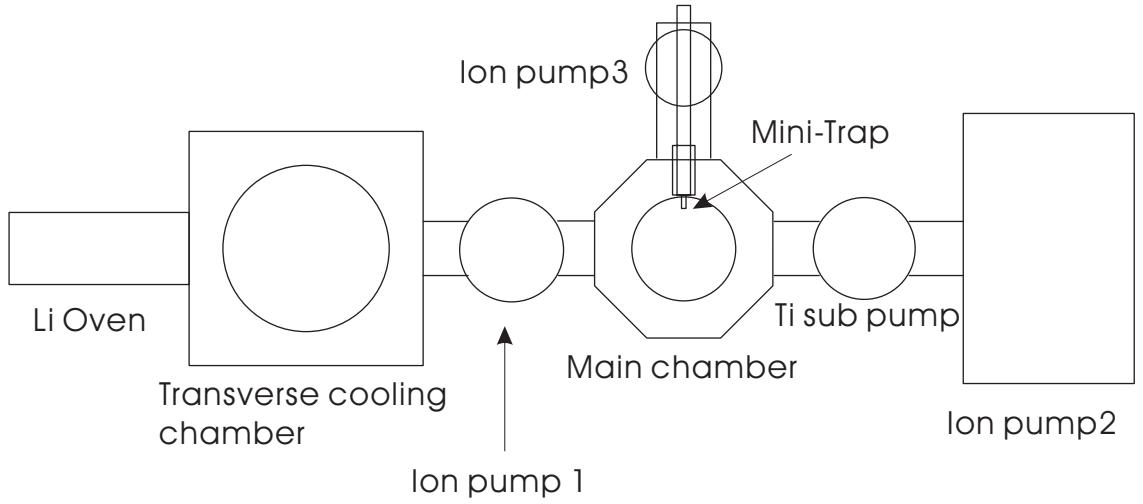


Figure 5.4: Vacuum Setup

The middle chamber is the chamber where we load the MOT and trap the Lithium in the Mini-Trap. The vacuum level here is extremely important because it will affect the MOT and the Mini-Trap life time. The MOT life time can affect the number of atoms loaded into the MOT. The Mini-Trap life time is one of the key parameters that determines if the evaporative cooling can be sustained. To maintain a very good vacuum in this chamber, we use a 20l/s triode ion pump (to pump noble gas better) together with a Ti sublimation pump (to better pump the Hydrogen). The upper chamber is where the current leads of the Mini-Trap stay, and although there is not much dirt in this chamber, the outgassing area is quite large. If we do not have a pump here to keep it at a reasonably low level, the throughput will all go into the main chamber and kill the vacuum in the main chamber. So we put a 8l/s ion pump in this chamber. The upper chamber and the left chamber are connected to the main chamber with a thin connection, which guarantees a good differential pumping that is enough to sustain 2 orders of magnitude of pressure gradient.

The vacuum level in the main chamber is roughly about 10^{-11} Torr inferred from the 87-second lifetime in the Mini-Trap.

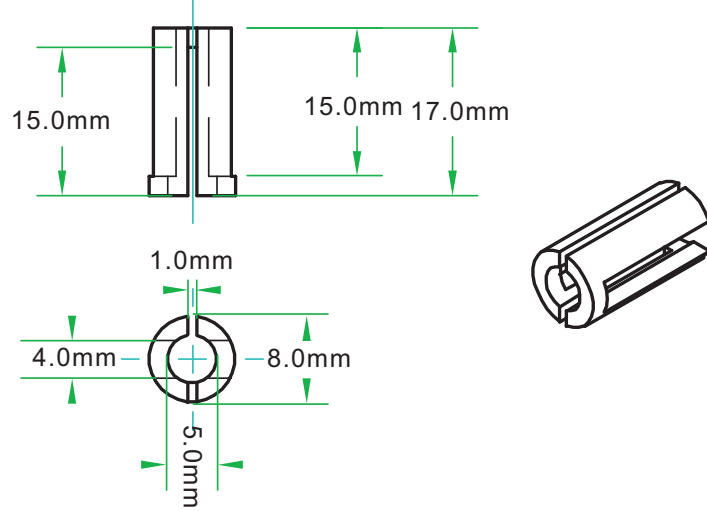


Figure 5.5: The Copper Piece

5.5 Mini-Trap Construction

The Mini-Trap is made of 4 parts, and the first part is shown in Fig. 5.5, made from a solid piece of oxygen-free copper. We start from a column that has a diameter of 8mm and height of 12mm, then we bore a hole of 5mm in the middle of the column. A window with a width of 4mm is cut from the side, and through the middle of the column, another 2mm wide slit is cut through the orthogonal direction to form the 4 Ioffe bars. At one end of the trap, the remaining partial ring forms the pinch coil. The other end of the copper piece is welded to a ceramic chip.

The ceramic chip is made from direct bond copper (DBC) chip. The process of DBC is performed by a spinel reaction between CuO and Al_2O_3 . In order to develop DBC on alumina substrate with high bonding strength, alumina substrate was preformed as follows: Cu was sputter-deposited on alumina substrate. The Sputter-Deposited Cu (SDC) on the alumina substrate was oxidized at 673K for 30min. in an air atmosphere and then stabilized at 1273K for 30min. in N_2 gas to improve bonding strength between preformed alumina substrate and SDC layer. Subsequently, the Cu-foil was bonded on preformed-alumina

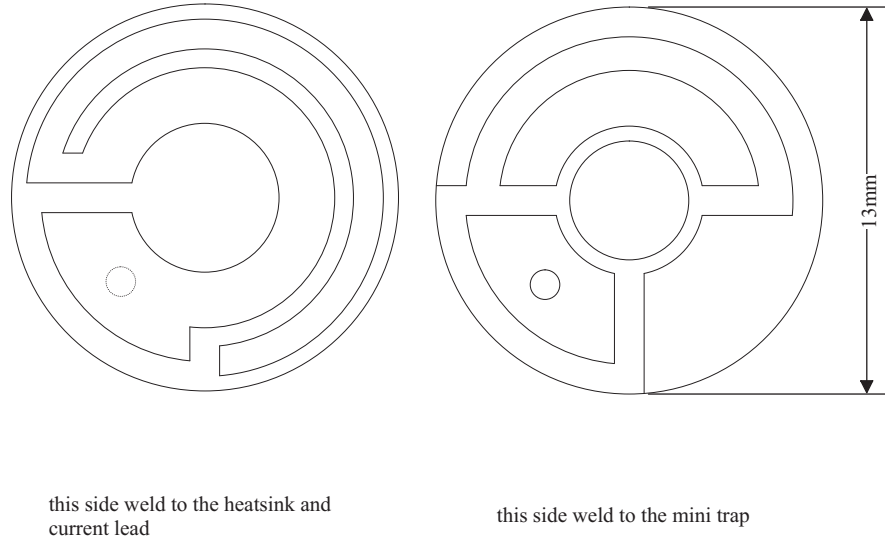


Figure 5.6: The DBC Chip

substrate in N_2 gas atmosphere at 1342 to 1345K. It was found that the optimum condition of DBC on the preformed alumina substrate could be successfully obtained at 1345K for 30min. Consequently, the bonding strength of DBC on the alumina substrate was the high value of 80N/cm. Observation and analysis of microstructure for Cu sputtered DBC showed that reaction compounds such as $CuAlO_2$ and $CuAl_2O_4$ formed in the vicinity of interface between Cu and the alumina substrate. Compared to some other mature micro fabrication approaches such as the thin film process and the thick film process, DBC provides the best thermal conductivity property and allows for the biggest carrying current on the copper layer. The schematics of the DBC chip is shown in Fig. 5.6.

In the middle of Fig. 5.6, a little disc is polished to form a mirror that can be used to set up an optical lattice. The little hole on the pad provides an electrical connection between both sides of the chip. The outer trace is welded to the “+” lead of the power supply.

In Fig. 5.6, the inner ring has the same diameter as the copper piece and work as the other pinch coil for the Ioffe-Pritchard trap. The outer ring is welded to the “-” lead of

the power supply and the heat sink.

The third piece of the assembly is the “-” current lead and the heat sink. Its geometry is shown in Fig. 5.7. The middle of the lead is hollow and can be water cooled.

The fourth piece of the assembly is the “+” current lead. It is concentric with the “-” current lead. Its geometry is shown in Fig. 5.8.

The assembly of the current lead and the heat sink is shown in Fig. 5.9

5.6 MOT Coils and Transfer Coils Assembly

The MOT coils run at 6A to provide a 10G/cm field gradient for the MOT. After the optical cooling and pumping, the current is snapped on to 40A in $1ms$ to transfer the atoms to a Quadruple trap at roughly a mode matching condition. Then the current is ramped down in $100ms$, and the current in the lower set of the transfer coils is ramped up to 200A, and the atoms are adiabatically transferred to the elongated Quadruple trap formed by the lower set of the transfer coils. In the next $200ms$, the current in the upper set of coils is ramped up to 200A and the current in the lower set of coils is ramped down, this shifts the atom cloud upwards, and when it reaches the center of the Mini-Trap, the current in the transfer coils are turned off in $2ms$ and the current in the Mini-Trap is turned on in $2ms$. This time scale is long compared to the radial oscillation frequency of the Mini-Trap, but short compared to the axial oscillation frequency, so the transfer is adiabatic in the radial direction and the loss of density in the axial direction is not very significant .

Because the whole transfer process only lasts less than $300ms$, the heat dissipation in the coils is very small, and we can use much thinner wires compared to the big water cooled coils in the traditional coils. The MOT coils are built with 13 layers of AWG 14 square section wire, and each layer has 6 turns. The transfer coils are built with 4 layers of AWG 14 square section wire, and each layer has 4 turns. The MOT coil current density is much lower than the transfer coil because we want it to run a continuous current of 6A for the

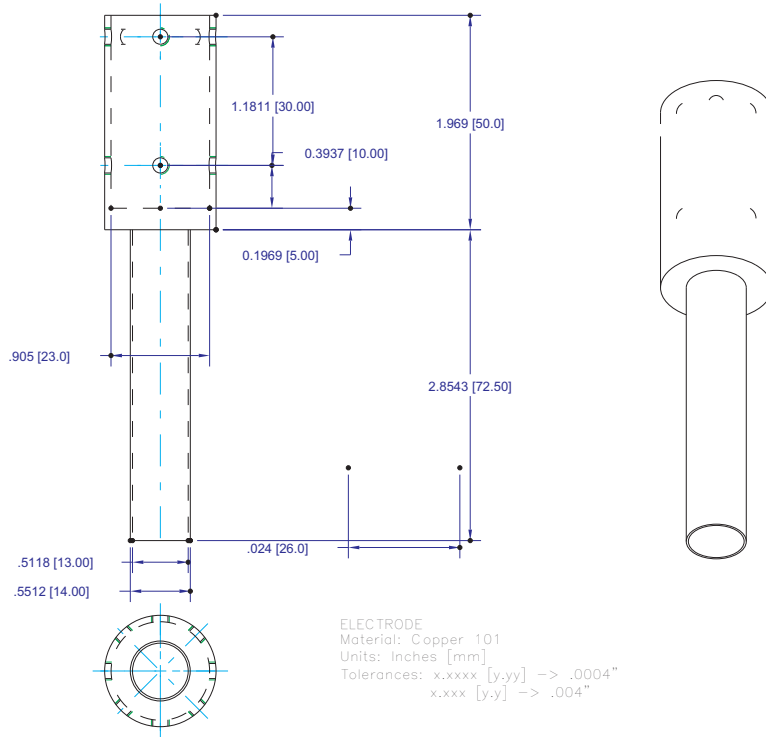


Figure 5.8: the + current lead

MOT without water cooling. Under these transfer currents, the temperature rises in both the MOT coils, and the transfer coils are minimum, and it does not raise the temperature in the chamber to affect the vacuum level.

The Geometry of the MOT coils and the transfer coils are shown in Fig. ??

5.7 Power Supply and Current Switches

The power supply and switching circuits are relatively easy to build due to the low power dissipation. In this section, I will introduce them with the corresponding circuit diagrams.

The most complicated one is the power supply for the MOT coils. Its schematics are shown in Fig. 5.10.

During the MOT loading, switch Q2 is off and switch Q3 is on, the MOT coil is powered by a low voltage 4V power supply B3, and the current is 7A. At the end of the MOT loading

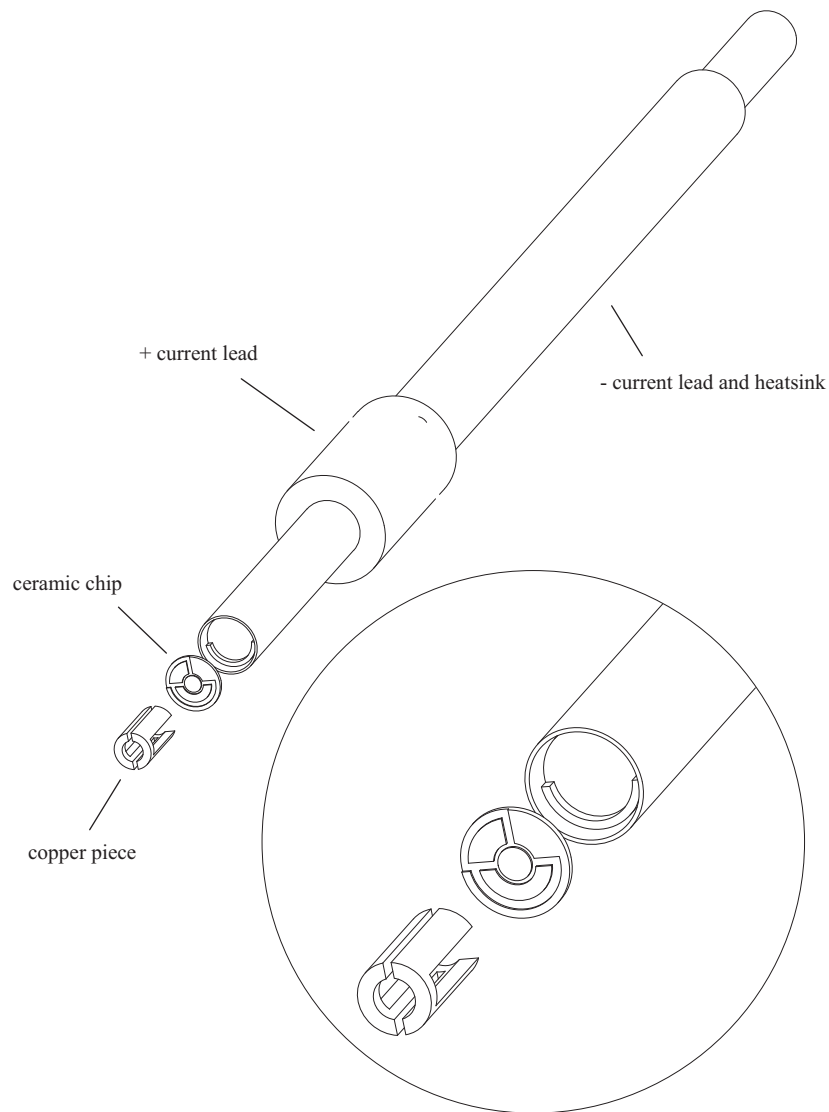


Figure 5.9: The Assembly Diagram

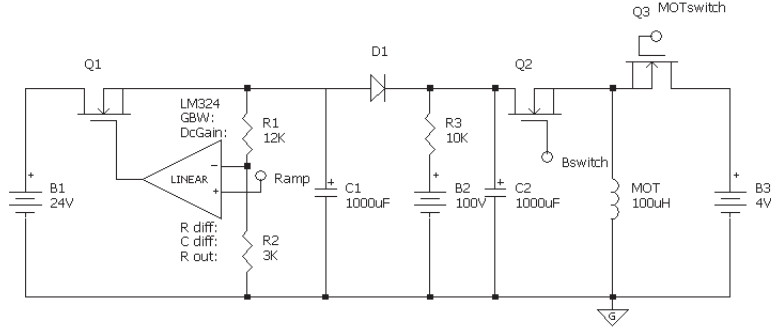


Figure 5.10: Schematics for the MOT Coils

and Doppler cooling, Q3 is turned off for the pumping, when a $300\mu s$ pulse of 10G bias field is on for the optical pumping. After the pumping, Q2 is turned on, and capacitor C2 will discharge through the the MOT coil right away. C2 is charged to about 100V during the MOT loading in each cycle by the power supply B2. When Q2 is on, the current in the MOT coil will rise to the peak of 40A in less than $1ms$, which is determined by the inductance of MOT coil and the capacitance of C2. Without this discharging circuit, the current in the MOT coils will take much longer to ramp to 40A; this will cause phase space density loss of the atoms after they are transferred into the Quadruple trap. The voltage of power supply B2 has to be properly adjusted for different Quadruple currents to avoid the current overshoot.

Power supply B1 is made of 2 car batteries. Car batteries are very cheap to operate and they can output huge currents in a short period of time. 600A is easy for a single car battery, and if connected in parallel, several kilo Amperes are not hard to achieve. In our case, we only use it at 40A. Q1, R1, R2, C1, and the OP amp form a very simple yet

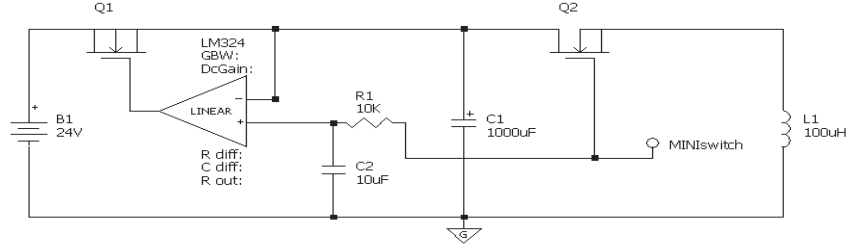


Figure 5.11: Schematics for the Mini-Trap

nice voltage regulator, and the output voltage is controlled by the input at the positive input of the OP amp. The ramping speed of the power supply can be less than $1ms$, more than enough for our transfer speed of $100ms$. The big capacity C1 effectively suppresses the close loop gain of the feed-back loop at a higher frequency to eliminate self excited oscillation, this is why a voltage regulator has a much faster ramping speed than a current regulator. D1 protects the voltage regulator and prevents the charging current of C1 back-flow into the regulator. Varistors are connected in parallel to switch Q2 and Q3 to protect the MOSFETs. The current in the MOT coils can be turned off in less than $50us$. The control signal for Q2 and Q3 comes from a pair of opto-isolators, because the source of both MOSFETs are not grounded.

The power supply for the Mini-Trap is shown in Fig. 5.11.

It also has a voltage regulator as the MOT power supply. This time, the input power supply is a HP 6671 power supply and its voltage ramping time is $50ms$, but when we transfer the atoms from the rectangular coils to the Mini-Trap, we want a semi adiabatic transfer, the Mini-Trap has to be turned on in about $2ms$. Direct ramping from the HP



Figure 5.12: Schematics for the Pumping Bias Coil and the Rectangular Coils

power supply is not fast enough, so we can also directly turn on the current switch; however, due to the very low self inductance of the Mini-Trap, the turn-on speed is $100\mu s$, which is too fast for the semi adiabatic transfer. So we use the voltage regulator again. When the Mini-Trap switch is on, the control voltage will charge the capacitor C2, and the voltage across C2 will ramp up exponentially with the time constant defined by R1 and C2. By adjusting either R1 or C2, we can adjust the turn-on speed of the Mini-Trap. The voltage across C2 will quickly ramp up to saturate Q1, then the current will be regulated by the HP power supply.

The HP power supply is controlled by a ramp voltage from a HP arbitrary wave function generator, which allows us to optimize the Mini-Trap current during the evaporative cooling process.

The power supply of the pumping bias coil and rectangular coils are shown in Fig. 5.12.

The pumping bias coil needs more than 100 A for only a few hundred micro seconds. It is overkill to use a big power supply just to power the bias field. Instead, we use a charged capacitor to supply the transient current. The capacitance of the capacitor is chosen to have a discharge time of about $500\mu s$, and we can adjust the charging voltage of the capacitor to adjust the peak current in the bias coil.

The switch circuit for the rectangular transfer coils are pretty simple. However, in

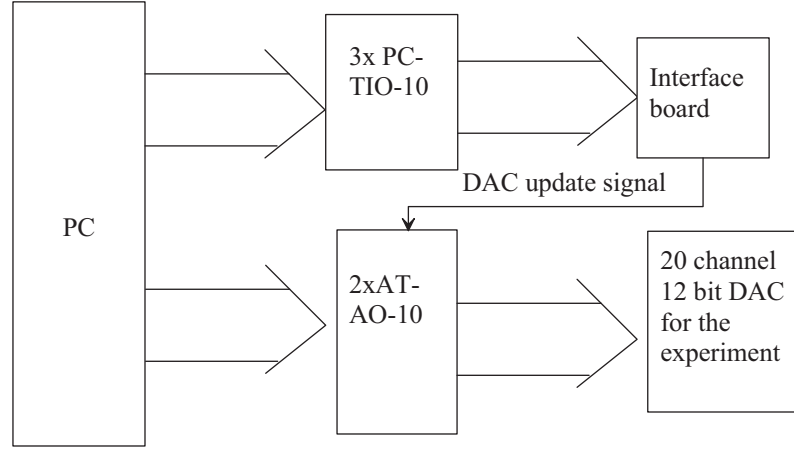


Figure 5.13: The Timing System

order to turn off the current in a few ms for the semi-adiabatic transfer, we have to play some tricks. If we just turn off the coils with the MOSFET switch, the switch-off time is less than $50\mu s$, which is too fast. The power supply (HP 6671) cannot ramp down in such a short period of time. We solve this problem by connecting a flying wheel diode parallel to the rectangular transfer coils. When the MOSFET switch is turned off, the current in the coils can keep flowing through the diode, and by using this approach, we can make the current turn off smoothly in $2ms$.

5.8 Timing and Control System

The real time control system is made with 3 National Instrument PC-TIO-10 timing boards and 2 AT-AO-10 DAC boards. A diagram of the timing system is shown in Fig. 5.13.

All the boards have a PC interface. Before the cycle runs, the boards are initialized and the registers and memory buffers on these card are programmed from a PC. Once the programme is done, during the timing cycles, the PC will do nothing to the timing and DAC boards. This pure hardware real timing system does not have the hard to determine software latency from a software based real-time system. The time resolution is below $1\mu s$,

which is more than enough for our system.

Each timing board has 2 AMD AM9513 timer chips and each timer chip has 5 timing counters, so one board can generate 10 timing edges. The timers are programmed from the PC. Every timer has a register to define the timing base and the overflow count number, which defines the counting time. Every timer is triggered by the overflow of its previous counter.

A home-made logic board takes all the overflow signals from the timers and outputs a raising edge for each timer overflow. This signal is used to trigger the DAC board to update its output.

The DAC board has a memory buffer where all the different DAC output values for each timing edge are stored. When the board receives a trigger signal from the logic board, they will update their output once, and thus with the trigger signal from the logic board, we can update the output voltages at each timing edge.

Each DAC board has 10 channels of 12 Bit DACs and can output a voltage between -10V to +10V. So our system has a 20 channel analog output.

One thing we have to be very careful of is when a very long time sequence is followed by a very short time sequence, because the long time sequence chooses a long timing base, and when the timing base is longer than the following time sequence, it will cover the output of the short time sequence. The cycle will miss one trigger, and this will totally screw up the timing and sometimes causes serious problems. When this happens, we add a bogus timing edge between the two timing edges, and the bogus will be longer than its previous timing base and short enough to avoid killing its following timing edge.

The drivers that talk to the board are written by Todd. Gustavson. He also developed a graphics interface for Windows 3.1. Later, Francesco Minardi recompiled the driver under Windows 98 and rewrote the graphics interface to add some useful options.

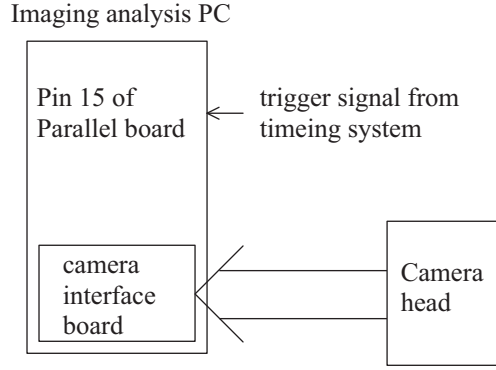


Figure 5.14: The camera diagram

5.9 Imaging System

We use both florescent and absorption imaging to measure the atom numbers and the size of the atom cloud. The camera we use is a Electrim (www.electrim.com) EDC-1000N CCD digital camera. The camera is very cheap, its CCD resolution is 652x494, the pixel size is 7.4um, and each pixel has an 8 bit resolution.

The camera package has a camera head and an interface board. The camera head and the interface board is connected with a 25pin D sub connector and the interface board is plugged into an ISA slot of the image processing computer.

Since we need to run the camera in the triggered mode, we have to use the only software module in the software package that comes with the camera. It is an .obj file that waits for a trigger signal from the parallel port Pin 15, and when the voltage on Pin 15 drops from 5V to 0V, the camera is triggered and the captured image is saved in an array in the memory. I wrote a DOS programme that saves the image in the memory into a file on the hard drive. The programme, camera.exe, has 3 input parameters, the first one is the offset for the pixel DACs, the second one is the gain for the pixel DACs, and the third one is the exposure time. The image file is written in the Matlab format, it can be easily loaded under Matlab and the image will be presented as a matrix. The subsequent image analysis is done in Matlab. The camera system diagram is shown in Fig. 5.14.

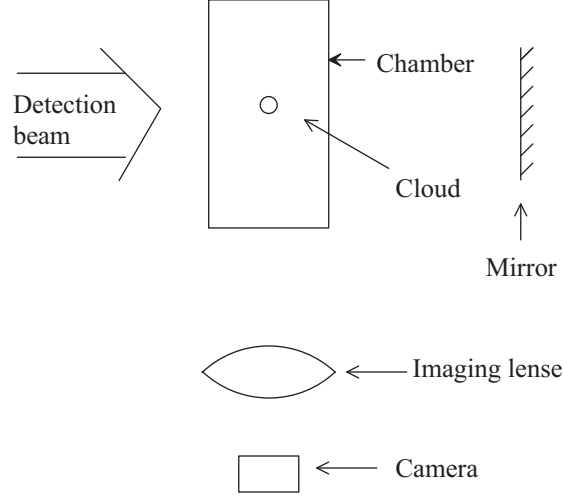


Figure 5.15: Fluorescent Imaging

5.9.1 Fluorescent Imaging

We do both fluorescent imaging from the MOT and from the Mini-Trap. The optical set-up for the fluorescent imaging from the MOT is shown in Fig. 5.15. A horizontal detection beam of $1/e^2$ diameter 2cm is overlapped with the horizontal MOT beam, and the polarization of the detection beam is opposite with the MOT beam. The power of the detection beam is 100mW, which is more than enough to saturate the optical transition from the ground to the excited states. During detection, the detection beam is turned on by an AOM for about 20 to $50\mu s$ depending on the number of atoms. The fluorescent light through the lower view port of the chamber is collected by a 4.6cm diameter lens with focal length of 7.5cm and projected onto the digital camera. The distance from the MOT to the lens is 21.4cm and the distance from the lens to the camera is 11.3cm, corresponding to an optical magnification of 0.53.

The scattering rate for a 2-level atom is

$$\frac{\gamma}{2} \frac{s}{1+s} \quad (5.1)$$

where s is the saturation parameter, and because the detection beam intensity is much greater than the saturation intensity of the atomic transition, the scattering rate is $\gamma/2$. The fluorescent energy collected into the camera is

$$E = \frac{\gamma}{2} N h \nu t_D \frac{\Omega}{4\pi} \quad (5.2)$$

where t_D is the detection time and Ω is the lens collecting solid angle. So,

$$N = \frac{8\pi E}{\gamma h \nu t_D \Omega} \quad (5.3)$$

The calibration of the camera is $E/I = 1.91 * 10^{-17} J/count$ for a gain setting of 200, where I is the integrated signal of the camera. The solid angle of the lens is calculated from the geometry to be $4\pi \sin^2 \frac{\theta}{2} = 0.036$, so the atom number is

$$N = \frac{8 * 3.14 * 1.91 * 10^{-17} * I}{2 * 3.14 * 5.9 * 10^6 * 6.63 * 10^{-34} * \frac{3 * 10^8}{.671 * 10^{-6}} * t_D * 0.036} = 1.2 * 10^3 * \frac{I}{t_D} \quad (5.4)$$

T_D is in the *ms*.

The optical setup for the fluorescent imaging in the Mini-Trap is shown in Fig. 5.16.

The detect beam has a $1/e^2$ diameter of 4mm. The detection power is 50mW, which is more than enough to saturate the atomic transition. The distance from the MOT to the lens is 23.4cm and the distance from the lens to the camera is 11cm, corresponding to an optical magnification of 0.47. The solid angle of the lens is 0.030. Because of the geometry limit, the upper half of the Mini-Trap is blocked by the chamber; so about half of the atoms cannot be detected, we put a estimated factor of 2 in the fluorescent imaging formula, the number of atoms in the Mini-Trap is.

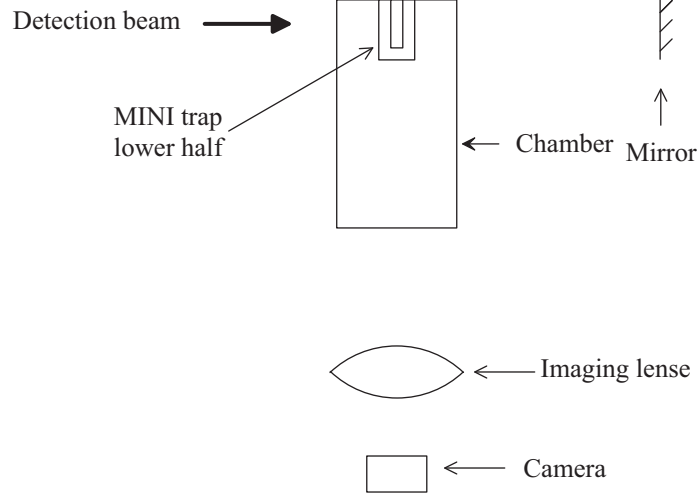


Figure 5.16: Fluorescent Imaging in the Mini-Trap

$$N = \frac{8 * 3.14 * 1.91 * 10^{-17} * I}{2 * 3.14 * 5.9 * 10^6 * 6.63 * 10^{-34} * \frac{3 * 10^8}{.671 * 10^{-6}} * t_D * 0.030} = 2.88 * 10^3 * \frac{I}{t_D} \quad (5.5)$$

When measuring the integrated signal I , it is very important to get rid of the background signal, as the back ground signal comes from scattered light and the bias setting of the camera. In the experiment, after the fluorescent detection is finished, we wait $2s$ to ensure there are no atoms left, then a second detection pulse is turned on for the same detection time as the first detection beam, and a second picture is taken. The subtracted images are used to calculate the integrated signal and the size of the cloud. The size of the cloud is obtained from a gaussian fit.

5.9.2 Absorption imaging

Absorption imaging is done only in the Mini-Trap. The optical setup is shown in Fig. 5.17.

The probe beam has a $1/e^2$ diameter of $15mm$. The probe beam power is $100\mu W$, and the pulse duration is $20\mu s$. Two imaging lenses both have a focal length of $150mm$. The

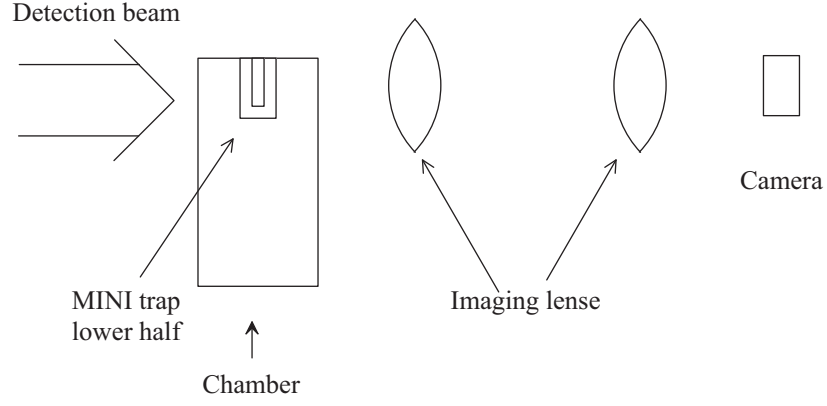


Figure 5.17: Absorption Imaging in the Mini-Trap

distance from L1 to the atom is $150mm$, the distance from the L1 to L2 is $300mm$, and the distance to the camera is $150mm$. The image on the CCD camera shows the shadow in the probe beam. The intensity of the probe beam after the cloud is

$$I(x, y) = I_0(x, y) \exp(-\sigma \int dz n(x, y, z)) \quad (5.6)$$

where $I_0(x, y)$ is the probe beam profile, σ is the absorption cross-section, and $n(x, y, z)$ is the atomic density distribution. In the image processing, the optical density $D_{optical}$ is calculated first from

$$D_{optical}(x, y) = -\ln \left[\frac{I(x, y)}{I_0(x, y)} \right] \quad (5.7)$$

from Eq. 5.6,

$$D_{optical}(x, y) = \sigma \int dz n(x, y, z) \quad (5.8)$$

It is easy to get the total number of atoms from

$$N = \int dx dy dz n(x, y, z) = \sum D_{optical}(x, y) \cdot \Delta x \cdot \Delta y / \sigma \quad (5.9)$$

where $\sum D_{optical}(x, y)$ is the integrated signal in the optical density plot. Δx and Δy is the pixel size of the camera, It is $7.4\mu m$ for our camera.

The absorption cross-section is

$$\sigma = C^2 \frac{\lambda^2}{2\pi} [1 + (\frac{\delta}{\gamma})^2] \quad (5.10)$$

where $\lambda = 671nm$ is the wavelength of the transition, $\gamma = 5.9Mhz$ is the line width of the transition, δ is the detuning of the probe beam frequency. C is the Clebsch Gordon coefficient. Since we use a linear polarized probe beam, the trapped states will quickly distributed onto all the $|F = 2 >$ states. We use an average squared Clebsch Gordon coefficient of $7/15$. The uncertainty of the distribution of atoms on the $|F = 2 >$ gives us an uncertainty of about a factor of 2.

One problem we faced is that the camera has a 8 bit DAC, It is sufficient to do the fluorescent imaging, but when we do absorption imaging, we have to divide the absorption by the background at a low background level, and this introduces a very big shot noise. In order to get rid of this problem, the images are first binned into 4×4 pixels in the imaging processing programme. This effectively increases the DAC from an 8 bit to a 12 bit DAC, and the shot noise is much smaller.

In the experiment, three images are taken, the first image $I_1(x, y)$ is taken in the the experiment sequence cycle with the atoms and the probe beam, and the second image $I_2(x, y)$ is taken 2 seconds after the first image, when all the atoms fly away. The third one $I_3(x, y)$ is taken before the cycle without the probe beam. The optical density is calculated by

$$D_{optical}(x, y) = -\ln(\frac{I_1(x, y) - I_3(x, y)}{I_2(x, y) - I_3(x, y)}) \quad (5.11)$$

By subtracting the third image I_3 , we effectively eliminate the noise from the scatter light and the bias of the camera, and this makes it possible to see a optical density of 4,

corresponding to 98 percent absorption.

5.9.3 Temperature Measurement from Free Expansion

From both fluorescent imaging and absorption imaging, we can deduct the size of the atomic cloud from the fit of the cloud profile. If we assume the initial cloud has a Gaussian density and velocity distribution, then after a free expansion t_1 , we have

$$x^2(t_1) = x_0^2 + \langle v_x^2 \rangle t_1^2 \quad (5.12)$$

where $\langle v_x^2 \rangle$ is the ensemble average of v_x^2 . If we choose a different expansion time t_2 , we have

$$x^2(t_2) = x_0^2 + \langle v_x^2 \rangle t_2^2 \quad (5.13)$$

From the previous equations, we have

$$\langle v_x^2 \rangle = \frac{x^2(t_2) - x^2(t_1)}{t_2^2 - t_1^2} \quad (5.14)$$

Then we can use

$$\langle \frac{1}{2} m v_x^2 \rangle = \frac{1}{2} K T \quad (5.15)$$

to deduce the temperature of the atomic sample.

$$T = \frac{m \langle v_x^2 \rangle}{K} \quad (5.16)$$

where $m = 1.65 \times 10^{-26} \text{ kg}$ and the Boltzmann constant $K = 1.38 \times 10^{-23} \text{ m}^2 \text{ kg s}^{-2} \text{ K}^{-1}$.

It is also easy to find the initial size of the cloud from

$$x_0^2 = \frac{x^2(t_1)t_2^2 - x^2(t_2)t_1^2}{t_2^2 - t_1^2} \quad (5.17)$$

A better way is to plot $x(t)^2$ at different expansion time, and then the slope is the average speed and the offset is the size of the cloud.

5.10 RF Evaporative Cooling Set-up

The RF evaporative cooling can be operated on the Zeeman levels or on the hyperfine levels. For the Zeeman level scheme, a radio frequency signal induces a two-step spin flip from $|F = 2, m_F = 2\rangle$ to $|F = 2, m_F = 1\rangle$ and from $|F = 2, m_F = 1\rangle$ to $|F = 2, m_F = 0\rangle$. The $|F = 2, m_F = 0\rangle$ is an un-trapped state and will leave the trap. The disadvantage of this approach is that an atom has to go through two steps to leave the trap, so the efficiency is lower. Also, this process generates $|F = 2, m_F = 1\rangle$ states and two atoms at this states could go through a collision and release the hyperfine split energy, and this will heat up the atom sample.

A better way is to use a micro wave signal which induces a transition from $|F = 2, m_F = 2\rangle$ to $|F = 1, m_F = 1\rangle$. The $|F = 1, m_F = 1\rangle$ is an un-trapped state and will leave the trap. In our experiment. we use this RF-evaporative cooling scheme.

The RF system set up is shown in Fig. 5.18.

We have a programmable arbitrary wave function synthesizer(HP8770A). It can be programmed from a GPIB bus and output either a constant frequency or a frequency ramp of arbitrary amplitude and phase. Unfortunately, the output frequency range is from 0 to 50 Mhz. In order to obtain the 800Mhz to 1Ghz, I made a frequency synthesizer that brings the frequency ramp of the HP8770A to a ramp from 800M to 1G. The center part of the electronics is a MC145170 PLL. MC145170 has two signal inputs, one is the external clock, which connects to the output of the HP8770A, and the other is connected to the output of the mixer. The mixer mixes the output of the VCO with an 800Mhz local

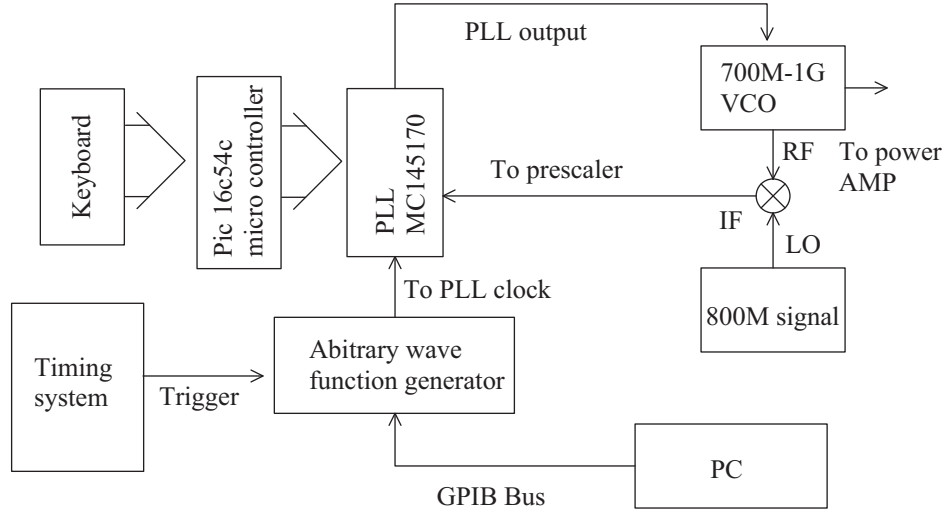


Figure 5.18: the RF Frequency Synthesizer

oscillator. The output of the VCO, which goes through a 200Mhz low pass filter, is sent to the PLL. This signal is down-scaled by the internal prescaler in the PLL and compared to the input signal from the HP8770A by a phase-frequency detector(PFD) in the PLL. The error signal, after going though a PI circuit, feeds back to the control lead of the VCO. The internal prescaler of the PLL can be programmed externally. In our circuit, we use a PIC 16c54c micro controller to programme the PLL. The PIC micro controller also works as a keyboard interface. The prescaler ratio is set by the keyboard every time the synthesizer reboots.

The output of the VCO is phase locked to the HP8770A and the output frequency is

$$f_{VCO} = 800 + n * f_{HP} \quad (5.18)$$

where f_{VCO} is the VCO output frequency, f_{HP} is the frequency of the HP8770A, and n is the prescaler ratio set by the keyboard, we usually use a ratio of 8.

The output of the VCO is sent to a 15W RF power amplifier. The output of the RF power amplifier connects to a RF isolator and to the RF antenna. The RF isolator

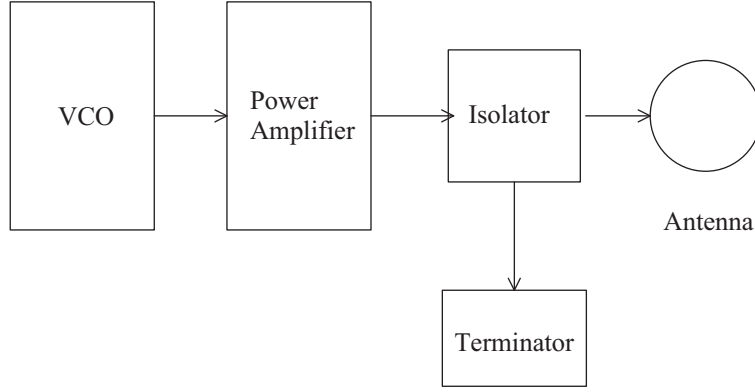


Figure 5.19: Antenna

has a input port which connects to the power amplifier, the second port connects to the antenna and the third port is terminated with a 50Ω load. The power from the input port is transmitted to the antenna, because the impedance of the antenna is much smaller than the 50Ω , and a large portion of the RF power is reflected back. The isolator will direct this power to the second port, which is terminated by the 50Ω load. This protects the power amplifier. The diagram of the antenna is shown in Fig. 5.19.

5.10.1 Temperature Measurement with RF Cut

The energy diagram of Lithium with respect to the magnetic field B is shown in Fig. 5.20.

For a certain RF frequency ν , an atom staying at a position with a local magnetic field B has a resonance condition of

$$h(\nu - \nu_0) = m_F g \mu_B B - m'_F g' \mu_B B \quad (5.19)$$

In the evaporation case, $m_F = 2, g = 1/2, m'_F = 1, g = -1/2, \nu_0 = 803.5 \text{ MHz}$ and $\mu_B/h = 1.4 \text{ MHz/G}$ the resonance condition becomes

$$\nu - \nu_0 = 2.1 \text{ MHz/G} * B \quad (5.20)$$

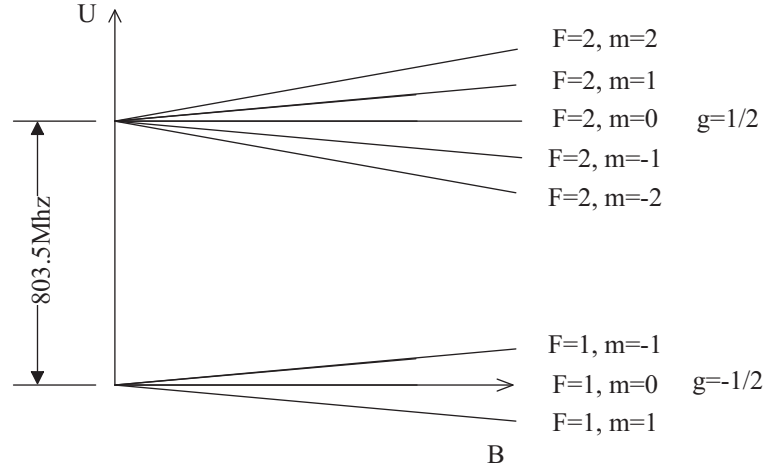


Figure 5.20: Energy Diagram

For an certain frequency ν satistying Eq. 5.20, any atom with energy high enough to reach a position with the local magnetic field B will become resonant with the RF signal and get kicked out of the trap. By applying different frequency cuts at ν , we can measure the number of atoms with a high energy $N(E > E(\frac{\nu - \nu_0}{2.1}))$. Ideally, this plot will be able to fit to the following function to find the temperature T as a parameter.

$$N(\nu) = N \left[E > E \left(\frac{\nu - \nu_0}{2.1} \right) \right] = N_0 \frac{\int_0^{2h(\nu - \nu_0)/3} \exp(-\frac{E}{k_B T}) dE}{\int_0^\infty \exp(-\frac{E}{k_B T}) dE} \quad (5.21)$$

where $E(\nu) = m_F g \mu_B B = m_F g \mu_B * \frac{\nu - \nu_0}{2.1} = \frac{2}{3} h(\nu - \nu_0)$

However, in practice, there are two difficulties. Firstly, Eq. 5.21 is not explicitly integratable. Secondly, due to power broadening and the re-thermalizing effect, the line profile will be a little different from that predicted by Eq. 5.21, and this has a significant effect on the fitting.

A better approach is to look at the following plot shown in Fig. 5.21, the shaded area is proportional to the average energy of the atoms in the trap. The area is not sensitive to the exact shape of the board line profile, so It is a much more precise way to measure the temperature.

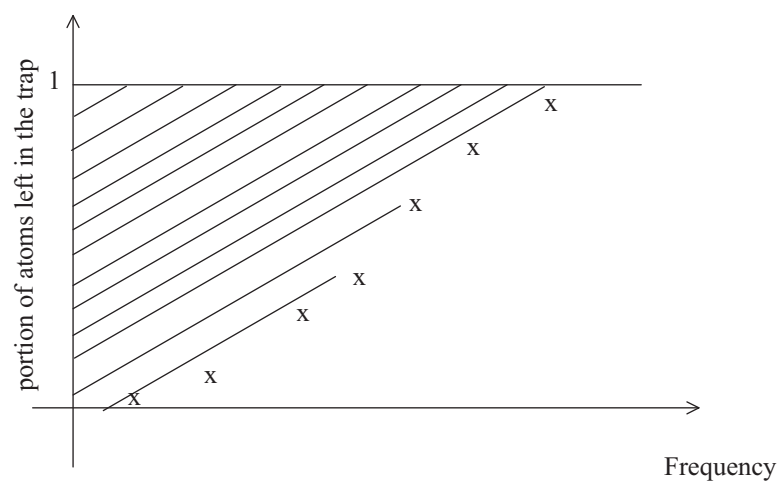


Figure 5.21: RF Cut Plot

Chapter 6

Experimental Results

6.1 Computer Simulation of the Mini-Trap

We used a simple model to calculate the magnetic field of the Mini-Trap. When calculating the field, we used 4 wires at the center of mass of the Ioffe bars to represent the 4 Ioffe bars. For the pinch coil, we used 4 short wire segments to represent the two arc segments. This would be sufficient for the center of the Mini-Trap because the distance from the Ioffe bars to the center of the trap is about $3.25mm$, while the size of wire around the center of mass is $\pm 0.75mm$, which is much smaller than the distance. The field at the edge of the trap is more likely to be different from the simulated value. A better method is to measure the field of the coil before it is put in the vacuum chamber, but the Mini-Trap is so small that we cannot find a small enough magnetic sensor that can precisely profile the magnetic field. Another method is to use the scaled up coil with the same geometry to simulate the Mini-Trap. But this requires a much larger current. It turns out that the simple model is pretty good. When we held the atoms in the Mini-Trap, we measured the trap depth and confinement of the Mini-Trap and it roughly agreed with the calculation.

The simulation of the magnetic field in the radial and longitudinal direction is shown in Fig. 6.1, Fig. 6.2, and Fig. 6.3.

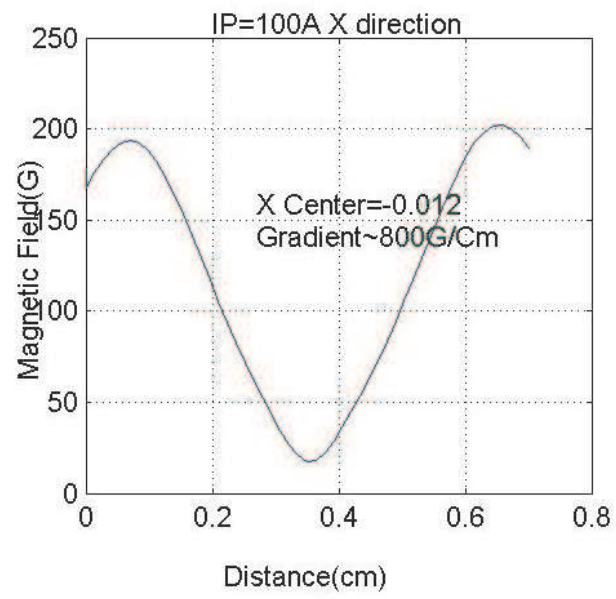


Figure 6.1: The Field of the Mini-Trap in the x Direction

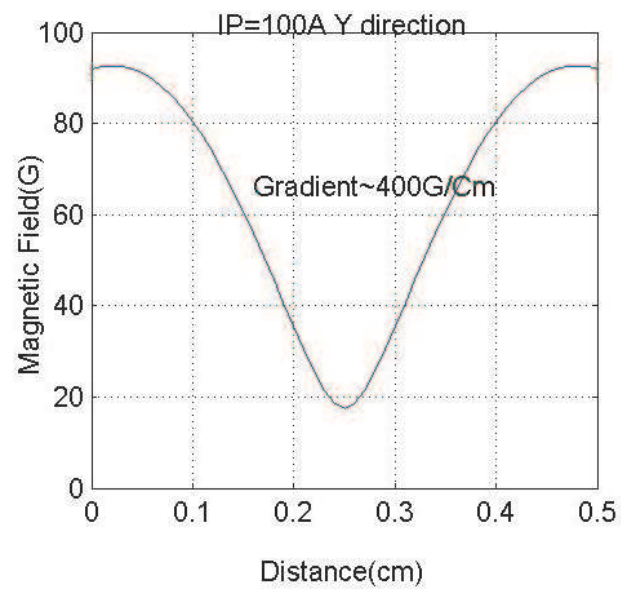


Figure 6.2: The Field of the Mini-Trap in the y Direction

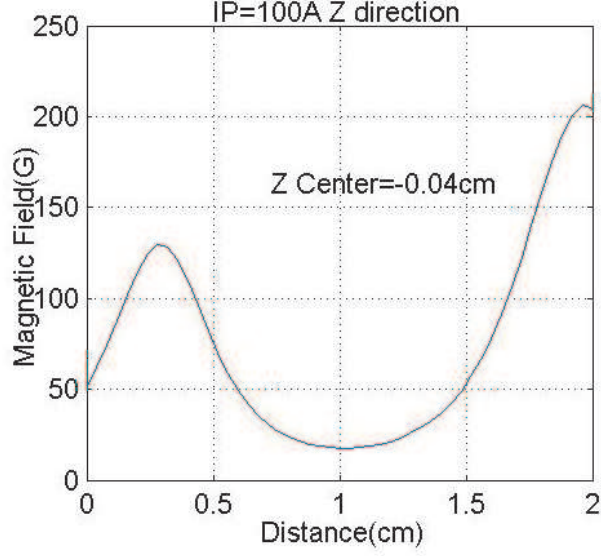


Figure 6.3: The Field of the Mini-Trap in the Axial Direction

All fields are calculated at 100A in the Mini-Trap. The asymmetry in the radial direction is due to the asymmetry of the Ioffe bars. Because we wanted to have a big numeric aperture in the x direction, where we do the absorption imaging, the distance between the Ioffe bars in the x direction is larger than that in the y direction. In the axial direction, the pinch coil at the tip of the Mini coil is only a partial of full circle, while on the back of the chip, there is a full circle of copper trace, so the field at the tip of the Mini-Trap is weaker than the field that is close to the chip. The gradient in the radial direction is about 400G/cm in the y direction and 800G/cm in the x direction. In the area near the center of the trap, because of $\nabla \cdot \vec{B} = 0$ and $\partial B_z / \partial z = 0$, $\partial B_x / \partial x = -\partial B_y / \partial y$, the gradient in the x and y direction is the same, the simulated value is 510G/cm. In the axial direction, the oscillation frequency is 67Hz. The trap depth is due to the saddle point in the y direction. When an external bias field is applied to lower the field in the center to 1G, the center field will be 1G, but the field around the saddle point remains roughly unchanged. The trap depth will be around 90G.

6.2 Vacuum Baking

Vacuum baking is very important to achieve a good life time in the magnetic trap. From the analysis of the run-away evaporative cooling, this is an extremely important variable we want to maximize. In the previous two Li BEC experiments, Hulet had a trap life time of $5Min$, which is one of the longest trap life time with a traditional chamber, and Salammon had a life time of $100s$.

When the vacuum system is assembled, we connect a turbo pump through a valve to the back port of the first ion pump, as shown in Fig. 5.4. The turbo pump is turned on with the valve closed and the bellow that connects to the valve is baked at $200^{\circ}C$. A spectrum analyzer is connected to the turbo pump assembly to monitor the partial pressure of the different gas components.

After the bellow is baked, we open the valve and start to bake out the vacuum system at $200^{\circ}C$ for several days. During the baking, we monitor the partial pressure of the remaining gas components. We also monitor the current in the ion pump controllers to track the vacuum level.

The current in the ion pump controller is about $100\mu A$ after the initial 2 hours of baking, then the current drops slowly. During the baking, the 3 filaments of the Titanium sublimation pump have to be degassed, and this is very important to reach the best vacuum. The filaments are baked at $10A$ for a few hours each, and when the filament is on, the current in the ion pump controller increases. It decreases while the outgassing process is going on, so it is important to wait for the current to stabilize and then switch to a different filament. It is also important to turn on the Lithium oven to bake out the dirt in the oven; we use a temperature of $350^{\circ}C$, which is $30^{\circ}C$ above the oven working temperature. Before baking the Lithium oven, we have a big concentration of N_2 from the spectrum analyzer, and after a few hours baking, the N_2 partial pressure drops several orders of magnitude and became much lower than the H_2 partial pressure.

After degassing of the Titanium sublimation pump filament, the pump is sputtered several times during the baking process. The current of the Titanium sublimation pump filament is turned to 50A for one minute. During the sputter period, the Titanium on the filament sublimates and the wall of the vacuum chamber is coated with a fresh thin layer of Titanium, which is a good absorber of most of the active gases (non-noble gas). The layer is an important absorber for H_2 , which is the major component of the remnant gas in the UHV (ultra high vacuum) environment.

The final ion pump current reading depends on the baking temperature and the area of the stainless steel wall of the chamber. In the building process, we replaced a small cross with a big cross, and this increased the wall area, and the final ion pump current increased from $3\mu A$ to $15\mu A$.

After the baking is turned off, the reading of the ion pump should be zero. Sometimes, the ion pump can have a leakage current, and this can be diagnosed by taking out the magnet of the pump and looking at the current in the pump. If the current has disappeared, that means the current is from a bad vacuum, and if the current does not change, then the pump has a leakage current.

After the baking, we have a pretty good vacuum. A quick check is done by monitoring the MOT life time. After the MOT is loaded, we close the oven shutter to block the incoming atomic beams and let the cloud decay under the back-ground collision. We have a long-term (short-term decay is dominated by light induced decay) decay time of 240s, which infers a vacuum level on the order of 10^{-11} Torr.

6.3 MOT Loading

Several factors affect the loading rate of the MOT and the maximum number of atoms in the MOT. In order to optimize these factors, we let the MOT load for 2s and looked at the fluorescence of the atoms from the the comb beams. Unfortunately, the two 45 degree

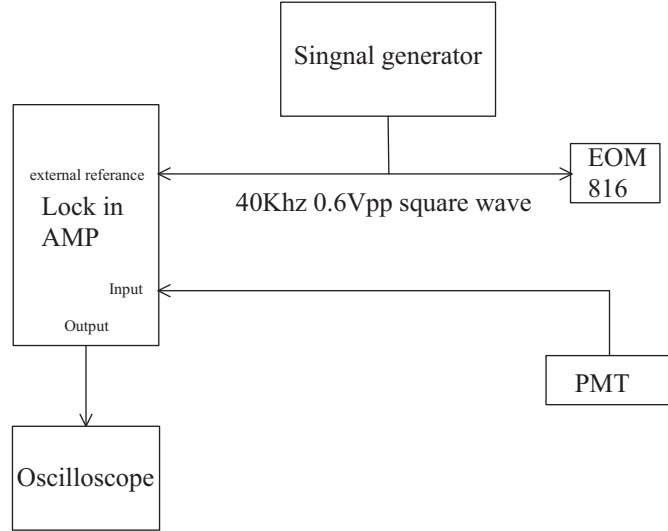


Figure 6.4: Loading Rate Measurement

vertical comb beams clipped on the Mini-Trap, and this introduced a strong scatter light to the photo multiplier tube(PMT), which we were using to monitor the fluorescence. The MOT fluorescent signals were totally submerged by the big background. We solved this problem by using a lock-in amplifier connected as shown in Fig. 6.4.

When the 816M EOM is turned on to 0.6V, the repumping light is on, and the laser interacts with the atoms, and we can see the fluorescent signal, but when the 816M EOM is turned off, the repumping light is off and the laser will pump all the atoms into the dark state quickly and stop interacting with the atom, so we cannot see the fluorescent signal. By modulating the EOM at 40Khz, the fluorescent signal will also be modulated at 40Khz. The lock-in amp will pick up this signal from the background and give a very clean loading curve.

The alignment of the transverse cooling does not seems very important to the loading rate, but the relative beam intensity distribution among the four transverse cooling beams is very sensitive. We optimize the loading rate by tweaking the power distribution with 3 half wave plates in the beam splitter system.

The detuning of the comb beam is quite sensitive and it can be easily optimized.

The current in the MOT coil is not very sensitive from 5A to 8A. We settled down at 5A.

The temperature in the Lithium oven is important, because when the temperature is too low, the vapor pressure is low and the incoming atomic flux is weak, and when the temperature is too high, the flux is strong, but the vacuum is bad. We chose a temperature of 320°C , which is close to the maximum loading rate, but still allows for a good vacuum.

The loading time constant is about 15 seconds, which is determined by the light induced loss. We chose a 30 second loading time for the cycle to ensure maximum loading.

The final number of atoms is also dependent on the size of the MOT trapping volume. This does not affect the loading rate, but it affects the final number of atoms. We looked at the stable value of the fluorescent signal on the scope. Because of the intersect of the Mini-Trap and the MOT beams on top of the MOT, we had to lower the center of the MOT coils a little to avoid the shadow of the Mini-Trap. This turned out to be very important for us to achieve maximum number of atoms. We optimized the center of the trap by changing the 3 pairs of bias coils to shift the position of the MOT center, and when we reached maximum loading, we marked the center of the trap on the camera and adjusted the bias coil to cancel the stray background magnetic field. After that, we adjusted the MOT coil to bring the center of the MOT back to the marked position and tweaked the bias coil again.

The current of the bias coils to cancel the stray background field is found by ramping the current in the MOT coil, and if the bias coils do not cancel the background stray field very well, we will see that the center of the MOT moves. If we adjust the current in the bias coil until the MOT shrinks but stays in the same spot, we can cancel the bias field very efficiently. This will ensure that we do not heat up the cloud when we transfer the atoms from the MOT to the Quadruple trap.

The loading rate is $2 * 10^8 \text{ atoms/second}$. At the end of the loading process, we have $2 * 10^9$ atoms in the MOT.

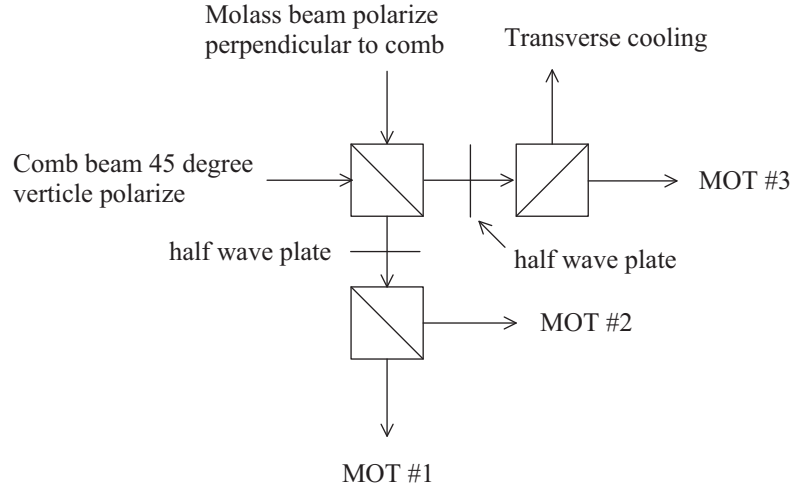


Figure 6.5: The Power Split and Combination of the Comb and Molasses Beam

6.4 Doppler Cooling

After the loading, the atoms are cooled by a near red detuned single frequency light. The oven shutter is closed, the comb beams are turned off by an optical shutter, and the cooling beam is turned on by an AOM, which is also used to control the intensity of the beam. The frequency can be adjusted by the double pass after the switch AOM. The repumper is no longer generated by the 816M EOM, instead, two stages of 200M double pass is used to get the repumper. This allows us to optimize the detuning and intensity of the cooling and repumping beam independently. The RF signal that drives the two 200M AOMs are identical, their frequency and intensity will control the intensity and detuning of the repumping beam. The cooling and repumping beams are combined by a polarization cube and fed into a fiber.

The output of the fiber is combined with the comb beam in the power splitter part, as shown in Fig. 6.5. The first polarization cube splits the molasses and the comb beam power into 50-50 on both output ports of the cube; the polarization of the molasses and the comb beam are orthogonal. The polarization of the two output beams are rotated by 45 degrees with a half wave plate, and now after a second cube, their power is also split

to 50-50, but now in the output beams, the polarization of the comb and molasses beams are the same. Three of the final doppler cooling beam is sent to form the MOT, and the last one is used for transverse cooling. This set-up overlaps two beams without sacrificing light power.

From Eq. 2.11, the temperature limit is reached when detuning is small. We optimize the intensity and detuning with two approaches. The first one is to measure the temperature and density with free expansion, described in section 5.9.3, and maximize the atom number and the density. The second one is to optimize the number of atoms transferred into the Mini-Trap. Because the uncertainty of the temperature measurement with free expansion is big, the second approach is better.

The optimized detuning is $\Delta = -\Gamma$; this is the best trade off between the trap loss and the cooling effect. If the detuning is smaller, the temperature of the atoms after cooling is lower, but because of greater light induced loss, we lose a lot of atoms during cooling. If the detuning is larger, we do not lose atoms but the cooling does not work well and we lose atom density. The optimal cooling beam intensity is $0.51mW/cm^2$, which is also a trade off between atom loss and cooling effect. If the intensity is too big, we lose a lot of atoms due to light-induced loss, and if the intensity is too small, we do not lose atoms, but the spring constant of the MOT is too small and we lose density. The detuning and intensity of the repumping light is not as critical as the molasses beam to the cooling. We find the optimal detuning is $\Delta = -2\Gamma$ and the optimal intensity is $0.17mW/cm^2$. During the cooling, we lose 20 percent of atoms in the MOT. At the end of the cooling, the temperature is $600\mu K$, measured with free expansion.

6.5 Optical Pumping

During the optical pumping, we first turn off the cooling beam, the remaining repumping light pumps all the atoms in the MOT to the $|F = 2 >$ hyperfine state. After 0.1ms, the

σ^+ diode laser light is turned on for $0.2ms$ to do the Zeeman pumping, a bias magnetic field is applied during the pumping period. The bias coil is made of 9 turns of coil with a diameter of $20cm$, and placed $20cm$ from the center of the chamber. The set-up is shown in Fig. 6.6. Ideally, all the atoms will be pumped into the $|F = 2, m_F = 2\rangle$ dark state and this is the state we will trap. We optimized the pumping parameters by maximizing the atom number transferred into the Mini-Trap.

The pumping beam detuning is critical to the pumping efficiency, especially when measured in the Mini-Trap instead of the Quadruple trap. We find the optimum frequency to be a 2 line width red to the $|F = 2, m_F = 2\rangle$ to $|F' = 2, m'_F = 2\rangle$ transition. The pumping bias field is critical to the pumping efficiency, and the optimum value depends on the detuning of the pumping beam. We find the intensity not very critical to the pumping efficiency. The optimal hyperfine pumping beam intensity is $1mW/cm^2$ and the Zeeman pumping beam intensity is $0.2mW/cm^2$. The pumping time is also not very critical; we left the hyperfine pumping beam on for a total of $0.3ms$ and Zeeman pumping beam on for $0.2ms$, the bias field is from the discharge of a capacitor to the bias field. The oscillation half cycle is $0.5ms$, the end of the bias field overlaps with the Quadruple trap for $0.1ms$, this assures that the atom spin smoothly follows the magnetic field.

We achieve a pumping efficiency of 35%, and this is measured by comparing the fluorescent signal of the atoms in the MOT and the atoms that transferred into the Quadruple trap. If we do not have the Zeeman pumping, the efficiency is 25%, which is about 60% smaller than with the Zeeman pumping.

6.6 Transfer to the Mini-Trap

After the pumping, all the light beams are turned off with optical shutter. It is very important to have a perfect light shield to maximize trap life time. Shutting off the AOM RF signal will not be good enough to eliminate the residue light, which can easily make

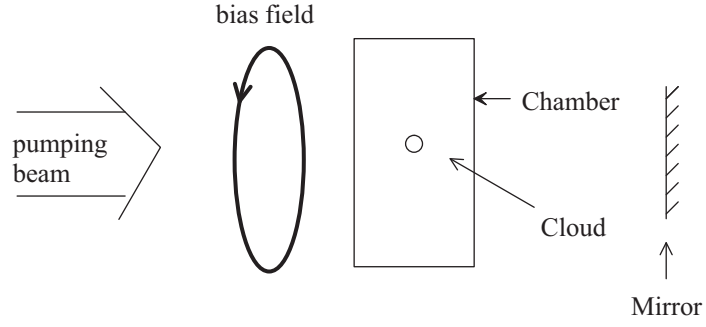


Figure 6.6: Optical Pumping Setup

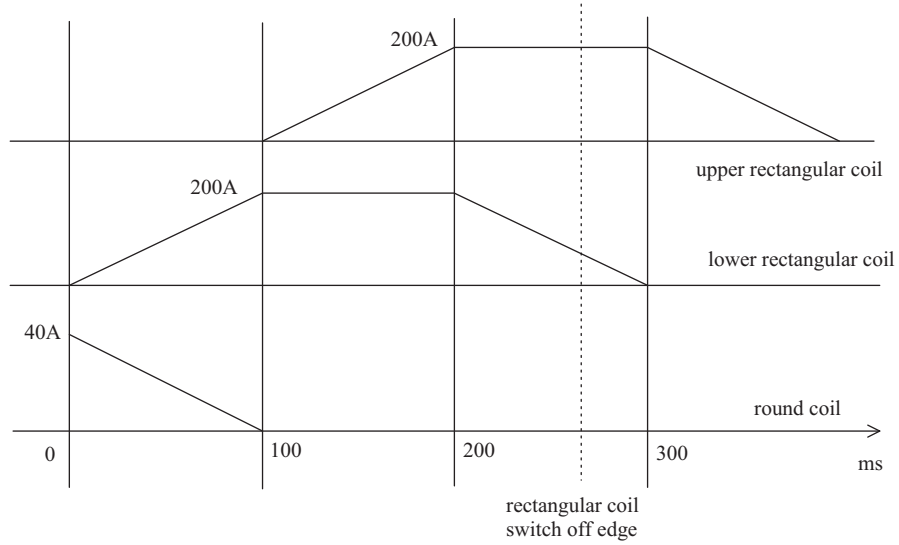


Figure 6.7: Timing Sequence of the Current Ramps

the life time of the trap drop to less than 1 second.

The round and rectangular quadruple coils then go through a series of ramping and the atoms are transferred into the Mini-Trap. The current ramp is shown in Fig. 6.7.

The current in both sets of the rectangular coils are switched off at the same timing edge. By adjusting the position of this timing edge, we can control the relative current in the lower and upper rectangular coils, and thereby we can thus adjust the position of the cloud. We tweaked this timing to align the vertical position of the cloud with respect to the center of the Mini-Trap. This parameter is very critical to the transfer efficiency from the

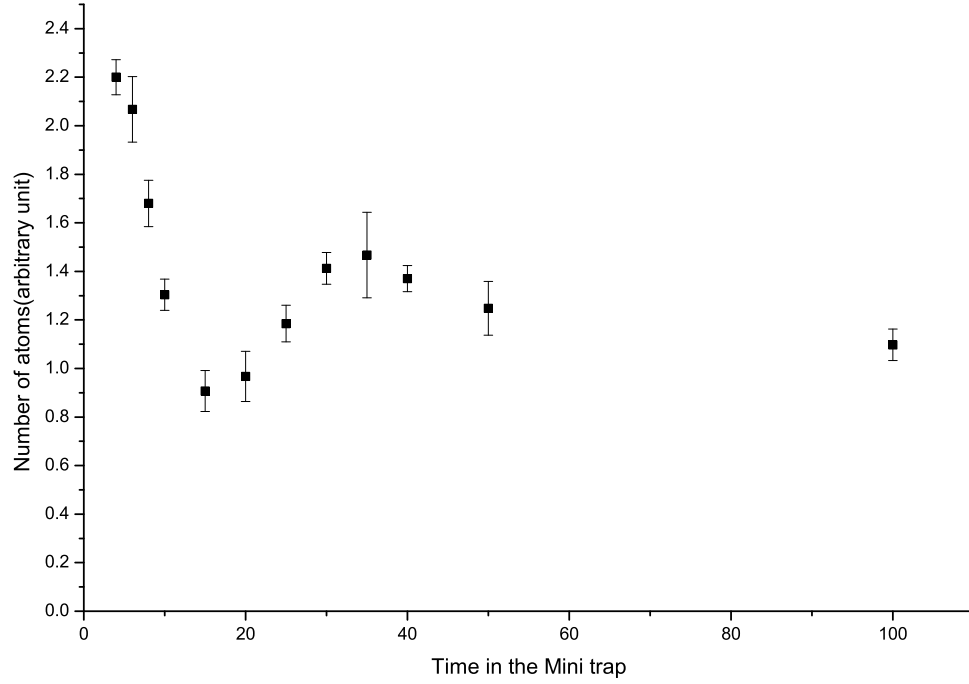


Figure 6.8: The Oscillation of Atom Cloud in the Mini-Trap

transfer coils to the Mini-Trap. If misaligned, the atoms will oscillate in the Mini-Trap, which is shown in Fig. 6.8. The horizontal axis is the time that the atoms stay in the Mini-Trap, the vertical axis is the atoms that are illuminated by a small beam on one side of the trap.

The transfer coils are mounted on a translation stage that can be fine-tuned along the direction parallel to the transfer coils. We tweaked the micrometer to align the transfer coils with Mini-Trap in this direction. It turned out that this parameter was very critical to the transfer efficiency.

In the other direction, the geometry is limited by the chamber and the mounting clamp. It turned out that the offset from the center was not very big.

The - current lead of the Mini-Trap is welded to a flange which connects to the vacuum

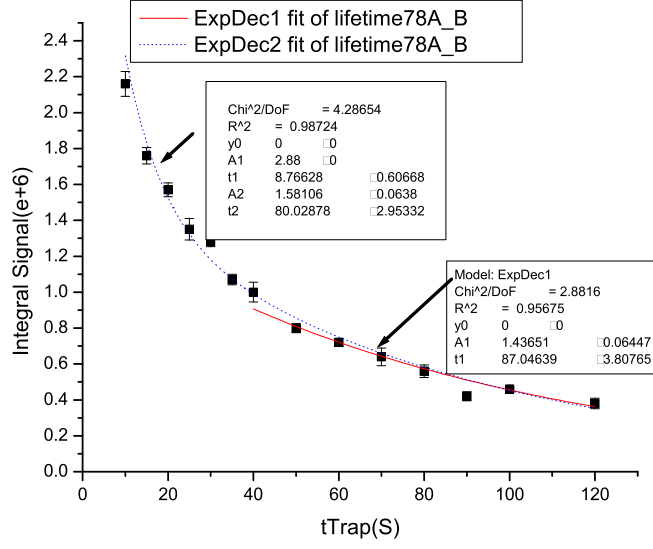


Figure 6.9: the decay of atoms in the Mini-Trap

chamber with a bellow, and its position can be adjusted by 3 micrometers. We can also use the micrometers to tweak the horizontal position of the Mini-Trap. However, the adjustment is not very smooth and repeatable.

We also optimized the transfer current of the Mini-Trap and found that the efficiency increased with the Mini-Trap until 150A, and since our trap life time becomes shorter at 150A, we set the transfer current at 100A. The final transfer efficiency is 25%.

6.7 Trap Life Time in the Mini-Trap

After the atoms are transferred into the Mini-Trap, the atoms will go through a fast loss followed by a slow loss; the decay is shown in Fig. 6.9. In the first 10 seconds, the atoms left the trap at a time constant of 8.7 seconds.

Two loss mechanisms contribute to this fast loss. First, there are some atoms with a higher energy than the lowest potential saddle point of the Mini-Trap. It take some time

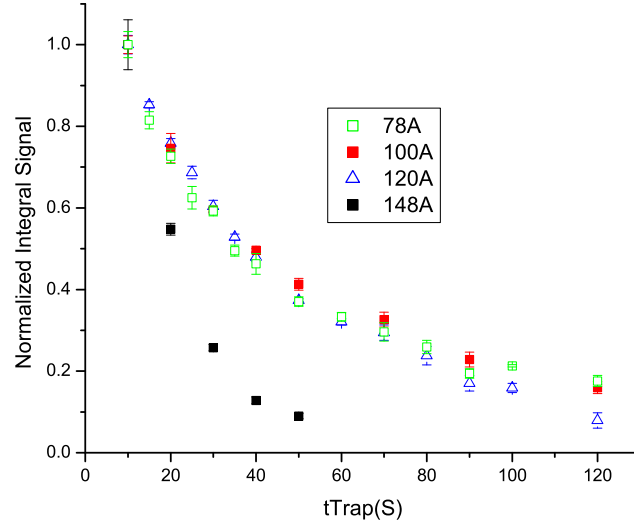


Figure 6.10: Comparison of Trap Life Time at Different Current

before they are able to find the saddle point and are lost. Second, there are elastic collisions that generate higher energy atoms and these atoms are lost from the trap.

About half of the atoms were lost in the first 10 seconds. After that, the atoms stay nicely trapped in the Mini-Trap. This slow decay is dominated by the background loss. The decay time constant is 87 seconds at 78A, which implies a good vacuum level.

The trap life time is comparable to typical trap life time in the traditional traps and is much bigger than the typical life time of 5 seconds in the microtrap.

The trap life time remains roughly unchanged with the trap current until it reached at about 120A, the trap life time at different currents are shown in Fig. 6.10

We have not decided the reason for the trap life time to drop around 150A. Heating of the Ioffe bars would be a possible explanation; however, according to our estimation, the rise in temperature at the tip of the Ioffe bars is less than $10^{\circ}C$ at 150A. Also it could be that the one turn trace on the DBC chip is overheating, because the current density is $140A/m^2$, which is much greater than that in the Ioffe bars.

6.8 RF Cut and Trap Parameters

10 seconds after the atoms are transferred into the Mini-Trap, we apply a constant frequency signal to the atoms for 4 seconds. The hyperfine split of the ground states is 803.5Mhz, and when we apply this frequency, no $|F = 2, m_F = 2 >$ atoms can go through a transition to the $|F = 1, m_F = 1 >$ untrapped state, because the bottom of the Mini-Trap is greater than zero. So all the atoms stay in the trap after the RF cut. When the cut frequency reaches

$$h(f_{cut} - 803.5) = (mg - m'g')\mu_B B_{bottom} \quad (6.1)$$

Suddenly, all the atoms can be pumped to the $|F = 1, m_F = 1 >$ untrapped state when they reach the trap bottom and are ejected from the trap. We have no atoms left in the trap. This sudden jump in atom number is very helpful to measure the magnetic field at the bottom of the trap.

The experiment data showing this sudden jump is in Fig. 6.11, and this is a cut for a Mini-Trap at current 89A. The sharp jump has a frequency resolution of less than 0.1Mhz.

From the jump frequency, and Eq. 6.3, we can calculate the magnetic field at the bottom of the trap by using

$$B_{bottom} = \frac{h(f_{cut} - 803.5)}{(mg - m'g')\mu_B} = 0.476 * (f_{cut} - 803.5)G/Mhz \quad (6.2)$$

We did several RF cuts for different Mini-Trap current, and plot it vs. the bottom frequency f_{bottom} as shown in Fig. 6.12. It is a perfect linear fit, which agrees with what we expected. However, one thing that we didn't expect is that the trap bottom of the Mini-Trap at 100A does not agree with the computer simulation. The simulated results is 17G, while the measured results is 7G.

The reason can be explained by the magnetic field caused by the current in the lead.

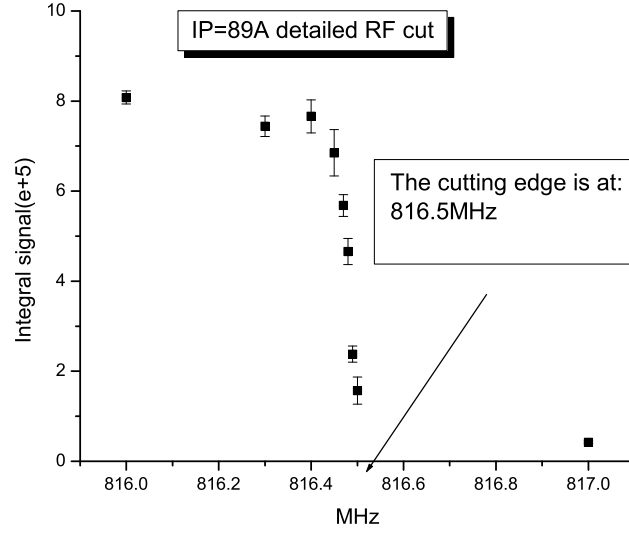


Figure 6.11: The Sudden Jump of Atom Numbers After the Cut

On the DBC chip, the current lead that feeds in and out of the current into the Mini-Trap is welded on an arc of trace on the chip, and part of the current that flows from the lead to the Mini-Trap actually flows from the trace and generates a magnetic field reverse to the pinch coil field at the trap center.

when the frequency of the RF cut is increased further, only atoms with energy

$$E = mg\mu_B B \geq mg\mu_B \frac{h(f_{cut} - 803.5)}{(mg - m'g')\mu_B} = 2 * h(f_{cut} - 803.5) \quad (6.3)$$

can reach the a spot with local field B and are resonant with the RF field and get kicked out. The RF cut data looks like Fig. 6.13.

Measured with the approach described in section 5.10.1, we found the temperature to be $510\mu K$.

The trap depth is measured by ramping down the current in the Mini-Trap to a very low value, which was 36A in our case. Then we started to do the RF cut, and we found that from 851.5Mhz to 857.5Mhz, we had different number of atoms left in the trap, while

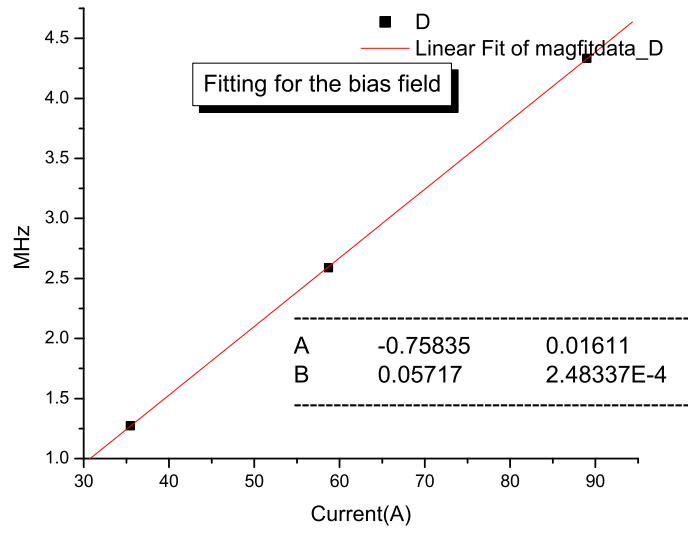


Figure 6.12: Mini-Trap Current vs. the Bottom Frequency

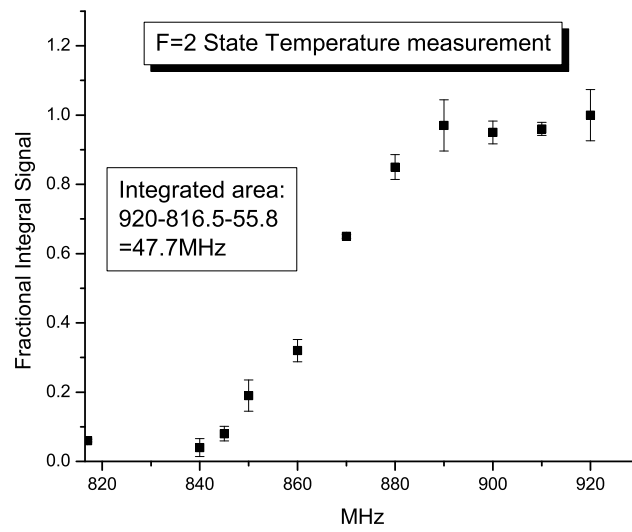


Figure 6.13: RF Cut and Temperature Measurement

from 857.5Mhz and above, the atom number left in the trap was almost unchanged. That means the trap depth corresponded to 857.5Mhz. The trap depth was calculated

$$\frac{857.5 - 816.5}{2.1} \frac{100}{36.22} = 66G \quad (6.4)$$

where 816.5 corresponded trap bottom. We scaled to 100A and found the trap depth to be 66G. This value is the lower bound of the trap depth. This value is pretty close to our calculated value of 70G. So we can assert that the Mini-Trap works as expected.

6.9 Absorption Imaging

The absorption imaging is taken when we turn off the Mini-Trap to avoid the Zeeman shift. A $10\mu s$ resonant detection pulse with a beam intensity of $100\mu W/cm^2$ is flushed on and image of the shadow of the atom cloud is projected on the camera. After the initial imaging process, as described in section 5.9.2, we have a nice absorption imaging of optical thickness, as shown in Fig. 6.14.

The plot of optical thickness along the horizontal and vertical direction is shown in Fig. 6.15.

Due to software issues, the optical thickness is magnified by 80 times. We can see that the maximum optical thickness is 3, which corresponds to a 95 percent absorption.

It is not a good idea to calculate the number of atoms at this big absorption level, even a small offset or noise can significantly change the optical thickness calculation.

In order to lower the optical thickness, we detuned the probe beam and plotted the integrated signal vs. the detuning in Fig. 6.16, all data points are half a line width apart.

We choose a detuning of -1.5 line width and incorporated the corresponding scattering cross-section at this detuning and found the total number of atoms to be $2 * 10^8$, which roughly agrees with the fluorescent imaging. We assume we only see half of the atoms both in the fluorescent and absorption imaging.

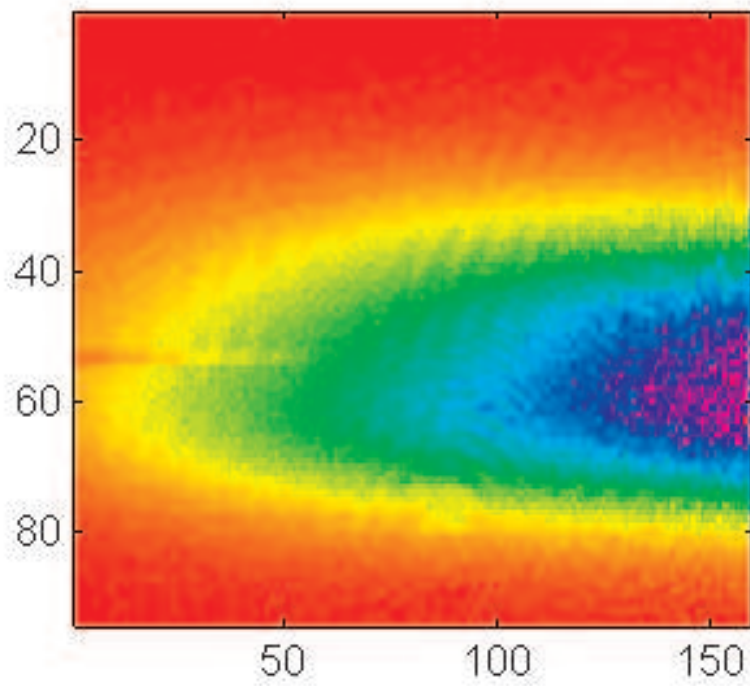


Figure 6.14: False Color Image of Absorption Image

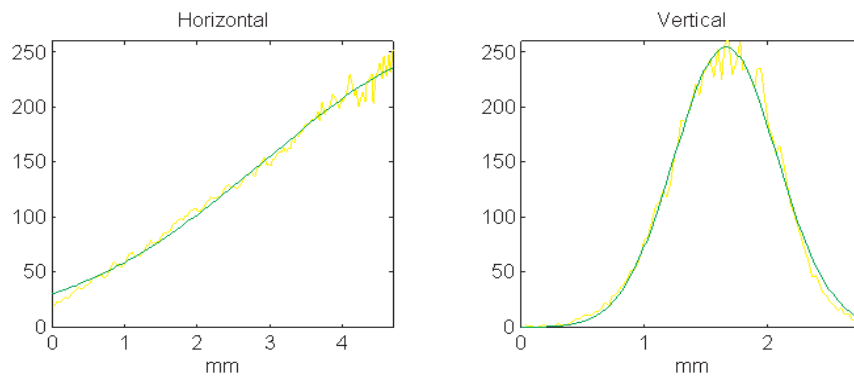


Figure 6.15: Gaussian Fit of the Cloud Optical Density. Note the horizontal fit only have half of the cloud because the other half of the trap is blocked by the vacuum chamber.

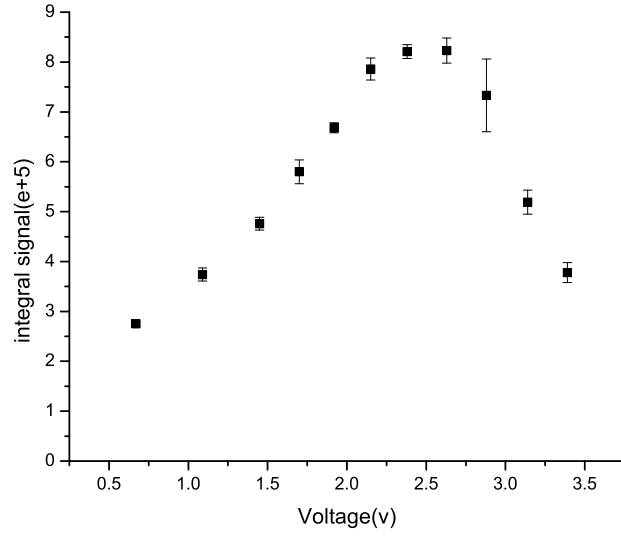


Figure 6.16: Absorption vs. Detuning

6.10 Evaporative Cooling

After the atoms are transferred into the Mini-Trap, we start to apply a RF ramp to evaporative cool the atoms.

The ramp is optimized in several steps, and each step is a linear ramp of the frequency. We started from an initial frequency of 1Ghz, and choose a fixed end frequency of 816Mhz. The whole ramp is divided into 3 segments. Both the end frequency and time duration of each segment are varied. The optimization was based on maximizing final peak optical density of the cloud. In a harmonic trap, the elastic collision rate is proportional to the peak optical density. This can be seen from below.

$$\Gamma = vn_0\sigma_{el} \propto \sqrt{T}N/(\sigma_x\sigma_y\sigma_z) \quad (6.5)$$

Because $\sigma_i = \sqrt{k_BT/m\omega_i^2}$, we have

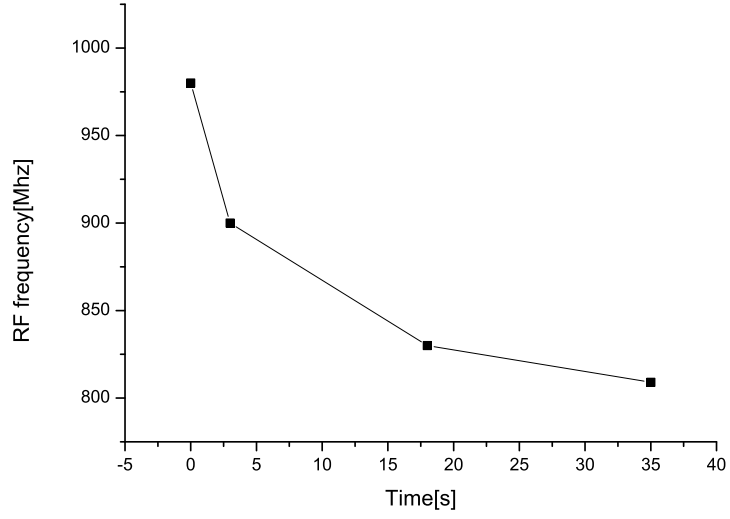


Figure 6.17: RF Cooling Ramp

$$\Gamma \propto N/T \quad (6.6)$$

Similarly,

$$D_{opt}(x=0, y=0) = \int dz n(x=0, y=0, z) \propto \sigma_z n_0 \propto \sigma_z N / (\sigma_x \sigma_y \sigma) \propto N/T \quad (6.7)$$

The optimized evaporative cooling ramp is shown in Fig. 6.17. The final result is not very sensitive to the exact shape of the RF ramp.

When changing the final cut frequency from 816Mhz to 805Mhz, the peak optical density does not change much, which indicates that the collision rate remains roughly constant, so the evaporative cooling is on the border of a runaway regime. The final result is sensitive to the initial number of atoms. A 60% gain in the initial number of atoms caused more than a 2-fold of gain in the final optical density.

6.11 Trap Oscillation Frequency Measurement With Parametric Heating

Parametric heating is the process during which the spring constant of a harmonic oscillator is modulated with ω .

$$k = k_0 + \delta k \sin(\omega t) \quad (6.8)$$

The energy of the system will show resonances at

$$\omega = 2\omega_0/n \quad (6.9)$$

in which ω_0 is the natural oscillation angular frequency, $n = 1, 2, \dots$. For a given amplitude of modulation of the parameter, the higher the order n of parametric resonance, the lower the energy that are delivered to the oscillator. So the most significant resonances are $\omega = 2\omega_0$ and $\omega = \omega_0$.

Parametric resonance is a very important tool to precisely measure the trap confinement. It has been used in both the Magnetic trap and the Optical dipole trap. However, because the Ioffe-Pritchard trap is not a very good harmonic trap, this approach only works when atoms are cooled to very low temperatures.

In our experiment, a 3A AC current is added to the 100A trap current by an audio amplifier. The atoms are cooled down first to 805Mhz, then a 10 seconds parametric process is turned on. If resonant, the parametric process heats up the atom sample and decreases the peak optical density. The $\omega = 2\omega_0$ and $\omega = \omega_0$ are shown in Fig. 6.18, Fig 6.19, Fig. 6.20, and Fig 6.21.

From the resonant frequency, we find the axial trapping frequency is 50Hz and the radial trapping frequency is 3kHz. From

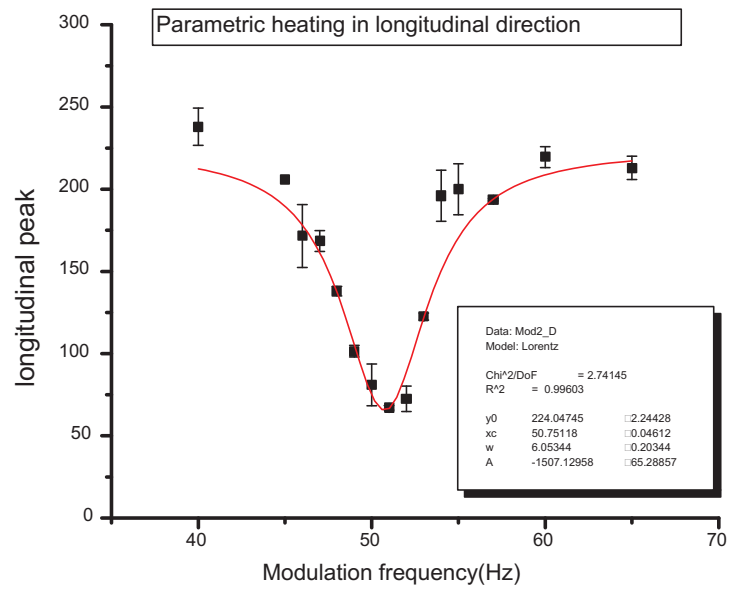


Figure 6.18: In the Axial Direction, $\omega = \omega_0$

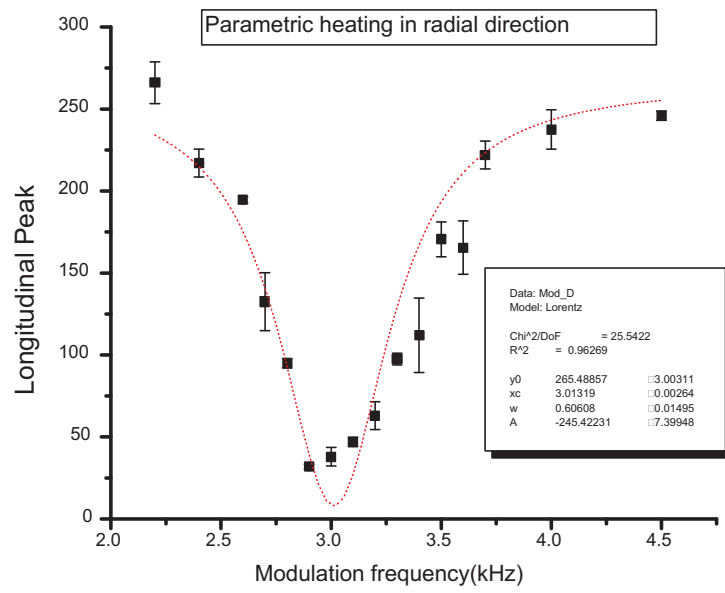


Figure 6.19: In the Radial Direction, $\omega = \omega_0$

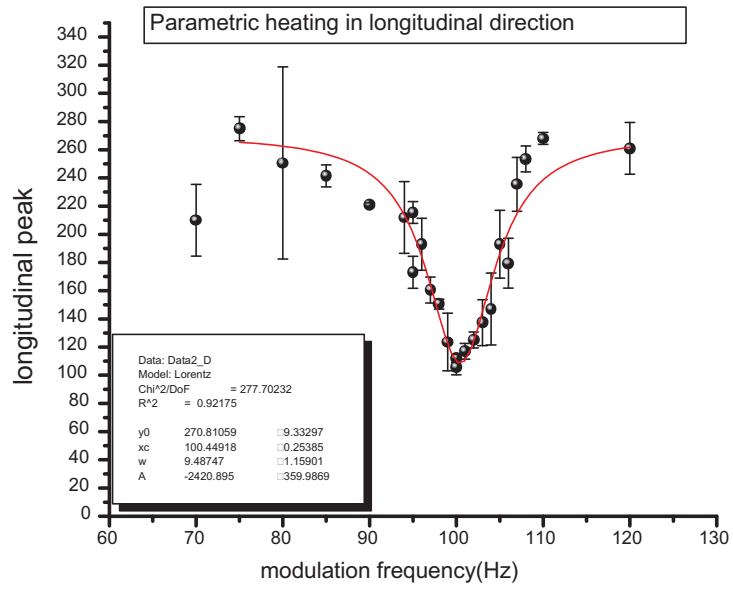


Figure 6.20: In the Axial Direction, $\omega = 2\omega_0$

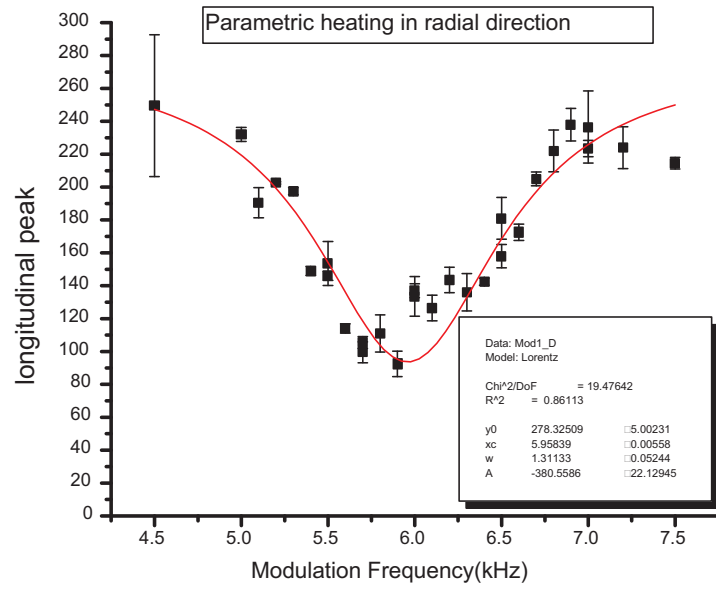


Figure 6.21: In the Radial Direction, $\omega = 2\omega_0$

$$\frac{\partial^2 B}{\partial z^2} = \frac{m\omega^2}{m_F g_F \mu_B} \quad (6.10)$$

and plug in $m = 1.152 * 10^{-026} kg$, $m_F = 2$, $g_F = 1/2$, $\mu_B = 9.274 * 10^{-24} J/T$, we can find the axial curvature is $122.6 G/cm^2$.

In the radial direction, similarly, we can get $\partial^2 B / \partial r^2 = 4.414 * 10^5 G/cm^2$. From Eq. 3.20 and $B_0 = 0.4 G$, we can find the radial magnetic field gradient $\partial B / \partial r = 420 G/cm$. The result reasonably agrees with the computer simulation.

6.12 Phase Space Density Towards BEC

After the evaporative cooling, the phase space density of the atoms increased significantly. We calculated the size of the cloud by fitting the *In situ* image to a Gaussian distribution. The temperature of the atoms is calculated from

$$T = \frac{m\omega^2 \langle x^2 \rangle}{K_B} \quad (6.11)$$

Peak phase space density ρ is calculated from

$$\rho = n_0 \lambda_{dB}^3 = N / (\sigma_x \sigma_y \sigma_z) * h / \sqrt{2\pi m k_B T} \quad (6.12)$$

The absorbtion images of various stages of cooling are listed below.

The corresponding atom number (N), axial size (σ_{axial}), radial size (σ_{radial}), and phase space density (PSD) at different final cut frequencies are listed below.

The radial size is too small when we ramp down below $808 MHz$, we infer its value using the axial size and assuming a constant aspect ratio.

The phase space density keep increasing when we further ramp down the RF cooling frequency and it pass 2.16 at around $6 * 10^4$ atoms, which indicate the formation of a BEC. The plot of phase space density vs atoms number is shown in Fig. 6.23. More detail



Figure 6.22: The absorption images at the final stage of the evaporative cooling. Because almost all of the upper half of the Mini-Trap is blocked by the chamber, we can only see half of the atom cloud. The absorption images is cut at the center. When the cloud is sufficiently small, we can see the whole atom cloud, as shown in the bottom picture. The center of the trap is decided at this stage.

final frequency(<i>Mhz</i>)	N	$\sigma_{axial}(\mu m)$	$\sigma_{radial}(\mu m)$	PSD
816	$6.2 * 10^6$	740	24	0.003
812	$4.4 * 10^6$	627	19	0.006
808	$2.2 * 10^6$	430	10	0.03
807	$1.2 * 10^6$	376	8.7	0.04
806	$1.01 * 10^6$	330	6.1	0.07
805	$3 * 10^5$	232	4.4	0.17

Table 6.1: Cloud parameters at different stage of cooling

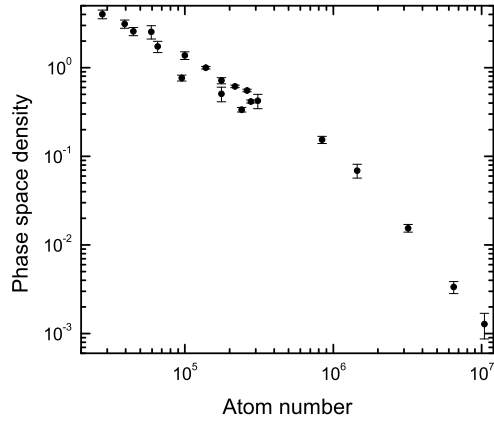


Figure 6.23: Phase space density vs number of atoms

will be included in my labmate Mingchang Liu's Ph.D thesis. Unfortunately, the negative scattering length of Lithium makes BEC unstable in free space, we can't release the trap and look at the condensate directly.

Chapter 7

Conclusion and Outlook

Our experiment in trying to achieve Lithium BEC started in 1998. The first set-up is a Quadruple trap and a so-called optical plug, a blue detuned dipole trap used to block the atoms from the magnetic field zero, which was used in Ketterle's first BEC experiment. This setup was unsuccessful because we did not have enough atoms in the MOT. At that time, we did not even have a transverse cooling stage, we only had $2 * 10^8$ atoms. The optical dipole trap was also too weak to block hot Lithium atoms, which cannot be cooled with sub-Doppler cooling.

The second version of our experiment was a TOP trap, and we added the transverse cooling, now we were able to get $2 * 10^9$ atoms. The TOP trap had a Quadruple trap gradient of $400G/cm$ and a TOP field of $70G$. The evaporative cooling never worked because of the shallow trap depth($18G$) and bad trap confinement in the initial cooling process when we needed full TOP field strength of $70G$ to hold the hot atoms.

Learning from the mistakes, we started to design a new trap in the summer of 2001, and the goal was to build a magnetic trap which would not only be capable of providing deep trap depth and good confinement, but would also be easy to build and run.

At that time, the Micro-Trap was very popular, but after some simulation, we found that the Micro- Trap was not good for Lithium. The limit was the small trapping volume

and short trap life time. One of the advantages of the Micro-Trap is its superior heat dissipation character. The micro wires are bonded directly to the substrate, and heat generated from the wires can be dissipated easily into the substrate, allowing for a huge current density.

When we designed our Mini-Trap, we kept heat dissipation in mind. In order to keep the total power dissipation low, a small trap has a huge advantage. Traditional big traps waste a lot of trapping volume because of the vacuum cell, and although the modern design of the traditional trap uses specially-made glass cells to alleviate this problem, but they are still limited. So we decided to build the trap inside the vacuum chamber. The trapping volume can thus be just as big as the size of the MOT, and it is still a good trade off between confinement(favor a small trap) and trapping volume(favor a big trap).

With the above considerations in mind, our Mini-Trap design gave great specs and successfully achieved Lithium BEC, a nasty atom due to the small elastic collision cross-section. At 100A, the radial gradient of our trap is $420G/cm$, and the axial curvature is $122.6G/cm^2$, which is better than most of the traditional big traps, but dissipates only 7W, 2 to 3 orders of magnitude lower than the traditional trap. The self inductance of the Mini-Trap is very small, and we can switch the trap on and off on the micro seconds level. Due to the low power dissipation, the current switch is very dependable, and we have never burned a MOSFET with the Mini-Trap.

The construction of the Mini-Trap is done with proven technology such as DBC (direct bond copper) and vacuum brazing (www.omley.com), which are highly compatible with a UHV environment. Due to the appropriate separation between the atoms and the surface of the wires, Mini-Trap has a minimum interaction between the atoms and the wires, and is immune to the problem faced by the Micro-Trap. We achieved over a minute lifetime in our Mini-Trap at 100A, which is much longer than the Micro-Trap.

One of the most important ideas in our experiment is the transfer of atoms from the Quadruple trap to the Mini-Trap. Small and tight traps usually suffer huge losses of both

atoms and phase space density during the transfer from the Quadruple trap to the Ioffe-Pritchard trap; the French Lithium group has only a 6% transfer efficiency from the transfer coils to the IP trap, and the phase space density loss is big, forcing them to introduce a laser cooling stage after transferring. Our setup uses the semi-adiabatic transfer, achieving around 25% transfer efficiency and minimal phase space density loss. Our evaporative cooling works right after the transfer.

We got the initial evidence showing evaporative cooling works last December, and in the beginning of this year, the Lithium in the apparatus ran out, which gave us the misleading sign that we had a bad vacuum, so we spent almost half a year figuring it out and we eventually made the system work again. We are improving the imaging system and will hopefully get better results. The Mini-Trap allows a theoretic diffraction limited spatial resolution of $1\mu m$, but our current imaging is not good enough to achieve this.

The Mini-Trap has huge potential in other BEC experiments too. To work with Rb, the Mini-Trap can be shrunk even further, allowing for an even higher current density and confinement. The Mini-Trap can be a portable system in a car, plane, or satellite. The Mini-Trap can also co-exist with Micro-Trap, working as a cold atom source for an atom chip. Due to the low power dissipation, the Mini-Trap can be cooled down to liquid nitrogen temperature. At this temperature, the electric conductivity of copper increases 8 times, and the thermal conductivity of the DBC chip increases 3 times. This allows for almost an order of magnitude of higher current density and a super tight trap.

There are many interesting experiments that can be performed on our current setup. Our current interest is focused on BEC of 7Li in an optical lattice. The scattering length of 7Li can be tuned by Feshbach resonance. A BEC of positive and negative scattering length atoms in an optical lattice behaves totally differently. For negative scattering length atoms, the ground state is a Schrödinger cat. Its very interesting to study the transition between these two systems with the help of Feshbach resonance.

We are looking forward to a great deal of exciting experiments in the next a couple of

years.

Bibliography

- [1] S. Chu et al., Phys. Rev. Lett. 55, 48 (1985).
- [2] P. D. Lett, et al., Phys. Rev. Lett. 61, 169 (1988).
- [3] J. Dalibard and C. Cohen-Tannoudji, J. opt. Soc. Am. B2, 1707 (1985).
- [4] E. Raab et al., Phys. Rev. Lett. 59, 2631 (1987).
- [5] M. Kasevich et al., Phys. Rev. Lett. 63, 612 (1989).
- [6] M. H. Anderson et al., Science 269, 198 (1995).
- [7] K. B. Davis et al., Phys. Rev. Lett. 75, 3969 (1995).
- [8] C. C. Bradley et al., Phys. Rev. Lett. 75, 1687 (1995).
- [9] T.-L. Ho and C. V. Ciobanu. Journal of Low Temp. Phys.135, 257 (2004).
- [10] E. Tiesinga, B. J. Verhaar, and H. T. C. Stoof, Phys. Rev. A47, 4114 (1993).
- [11] W. C. Stwalley, Phys. Rev. Lett. 37, 1628 (1976).
- [12] S. Inouye et al., Nature (London) 392, 151 (1998).
- [13] P. Courteille et al., Phys. Rev. Lett. 81, 69 (1998).
- [14] S. Jochim et al., Science 302, 2101 (2003).
- [15] M. Bartenstein et al., Phys. Rev. Lett. 92, 120401 (2004).

- [16] M. Greiner, C. A. Regal, and D. S. Jin, *Nature (London)* 426, 537 (2003).
- [17] M. W. Zwierlein et al., *Phys. Rev. Lett.* 91, 250401 (2003).
- [18] T. W. Hansch and A. L. Schawlow, *Opt. Comm.* 13, 68 (1975).
- [19] A. Migdall, J. Prodan, and W. Phillips, *Phys. Rev. Lett.* 54, 2596 (1985).
- [20] J. Gordon and A. Ashkin, *Phys. Rev. A* 21, 1606 (1980).
- [21] M. Kasevich and S. Chu, *Phys. Rev. Lett.* 69, 1741C1744 (1992).
- [22] A. Aspect et al., *Phys. Rev. Lett.* 61, 826 (1988).
- [23] A. Gallagher and D.E. Pritchard, *Phys. Rev. Lett.* 63, 957 (1989).
- [24] D. Sesko et al., *Phys. Rev. Lett.* 63, 961 (1989).
- [25] W. D. Phillips and H. Metcalf, *Phys. Rev. Lett.* 48, 596, (1982).
- [26] C. Monroe et al., *Phys. Rev. Lett.* 65, 1571 (1990).
- [27] V. Balykin, V. Lethokov, and A. Sidorov, *Pisma Zh. Eksp. Teor. Fiz.* 40, 251 (1984).
- [28] V. Balykin and A. Sidorov, *Appl. Phys. B* 42, 51 (1987).
- [29] A. Ashkin, *Phys. Rev. Lett.* 24, 156 (1970).
- [30] A. Migdall, J. Prodan, and W. Phillips, *Phys. Rev. Lett.* 54, 2596 (1985).
- [31] E. Majorana, *Nuovo Cimento* 9, 43 (1932).
- [32] P. Güttinger, *Zeit. Phys.* 73, 169 (1931).
- [33] J. Schwinger, *Phys. Rev* 51, 648 (1937).
- [34] I. Rabi, *Phys. Rev* 51, 652 (1937).
- [35] W. Petrich et al., *Phys. Rev. Lett.* 74, 3352 (1995).

- [36] Y. Gott, M. Ioffe, and V. Telkovskii, Nuclear Fusion Supplement 3, 1045 (1962).
- [37] V. Bagnato et al., Phys. Rev. Lett. 58, 2194 (1987).
- [38] D. Pritchard, Phys. Rev. Lett. 51, 1336 (1983).
- [39] T. Bergeman, G. Erez, and H. Metcalf, Phys. Rev. A 35, 1535 (1987).
- [40] M. Mewes et al., Phys. Rev. Lett. 77, 416 (1996).
- [41] T. Esslinger, I. Bloch, and T. Hansch, Phys. Rev. A 58 (1998).
- [42] L. Hau et al., Phys. Rev. A 58, R54 (1998).
- [43] Walraven, Proc. Scott. Univ. Summer Sch. Phys.44 (1996).
- [44] W. Ketterle and N. J. Van Druten, Advance in atomic, molecular, and optical physics, Vol. 37, 181.
- [45] O.J.Luiten et al., Phys. Rev. A 53,381 (1996).
- [46] T. Esslinger, I. Bloch, and T. W. Hensch, Phys. Rev. A 58, 2664 (1998).
- [47] A. S. Arnold, J. S. Wilson and M. G. Boshier, Rev. Sci. Instrum 69,1236 (1998).
- [48] C. J. Hawthorn, K. P. Weber, and R. E. Scholten, Rev. Sci. Instrum. 72 4477C4479 (2001).
- [49] L. Ricci, et al., Optics Communications 117, no.5-6, pp.541-549 (1995).
- [50] K. G. Libbrecht and J. L. Hall, Rev. Sci. Instrum. 64, 2133-2135 (1993).
- [51] H. F. Hess, Phys. Rev. B, 34,3476 (1986).
- [52] D. J. Wineland, Wayne M. Itano. Phys. Rev. A 20, 1521 (1979).
- [53] V. Vuletic, C. Chin, A. J. Kerman, and S. Chu. Phys. Rev. Lett. 81, 5768 (1998)

- [54] M. Zhu, C. W. Oates, and J. L. Hall. Phys. Rev. Lett. 67, 46 (1991)
- [55] W. Hansel, P. Hommelhoff, T. W. Hansch and J. Reichel Nature 413, 498 (2001)
- [56] H. Ott, J. Fortagh, G. Schlotterbeck, A. Grossmann and C. Zimmermann, Phys. Rev. Lett. 87 230401 (2001)
- [57] F. Schreck, G. Ferrari, K. L. Corwin, J. Cubizolles, L. Khaykovich, M. O. Mewes, and C. Salomon Phys. Rev. A, 64, 011402 (2001)
- [58] T. W. Hansch, I. S. Shahin and A. L. Schawlow, Phys. Rev. Lett. 27, 707 (1971)